PS1611.PDF [Page: 3 of 69]

DEFENCE R&D DÉFENSE

Statistics of SAR Interferograms with Application to Moving Target Detection

Christoph H. Gierull
Defence Research Establishment Ottawa

Defence R&D Canada

DEFENCE RESEARCH ESTABLISHMENT OTTAWA

TECHNICAL REPORT
DREO TR 2001-045
July 2001

National Defence Defense nationale

Canada

P516111.PDF [Page: 4 of 69]

105-03288/

DEFENCE R&D DÉFENSE

Statistics of SAR Interferograms with Application to Moving Target Detection

Christoph H. Gierull
Surveillance Radar Group
Aerospace Radar and Navigation Section

DEFENCE RESEARCH ESTABLISHMENT OTTAWA

TECHNICAL REPORT
DREO TR 2001-045
July 2001

Project
3DB29

Abstract

This report examines the statistics of the phase and magnitude of SAR interferograms towards the deployment of along-track interferometry (ATI) for slow ground moving target indication (GMTI). Great importance is attached to the practical applicability of the derived theoretical results, particularly with regard to the experimental MTI-mode of Radarsat2. Therefore, the results are evaluated with experimental airborne SAR data acquired during flight trials conducted in Petawawa in 1999. While the known probability density function (pdf) of the interferogram's phase (derived under the assumption of Gaussian backscatter) is shown to agree almost perfectly for a wide variety of backscatter conditions, the corresponding magnitude's pdf tends to deviate strongly in most cases. Motivated by this discrepancy, a novel distribution is derived for the interferogram's magnitude. This pdf, called the polynomial or p-distribution, matches the real data much more accurately, particularly for extremely heterogeneous composite terrain. Based on these statistics, a completely automatic detection scheme with constant false alarm rates for slow moving targets is proposed. All involved parameters required to determine the detection thresholds are estimated from the sample data. It is demonstrated on the basis of a real SAR scene that this detector is capable of detecting slow moving vehicles within severe ground clutter. Finally, practical aspects of the implementation and numerical stability are addressed, since many of the functions involved are comprised of indefinite power series which have to be handled cautiously.

P516111.PDF [Page: 6 of 69]

Résumé

Le présent rapport examine les statistiques de phase et d'amplitude des interférogrammes RAS en vue de l'application de l'interférométrie longitudinale (ATI) à la détection de cibles terrestres mobiles (GMTI) lentes. Une grande importance est accordée à l'applicabilité pratique des résultats théoriques dérivés, notamment à l'égard du mode MTI expérimental de Radarsat2. Par conséquent, les résultats sont évalués par comparaison avec des données d'un RAS expérimental aéroporté acquises lors d'essais en vol effectués à Petawawa en 1999. Alors qu'il est démontré que la fonction de densité de probabilité (pdf) connue de la différence de phase de l'interférogramme (dérivée en supposant qu'il y a rétrodiffusion gaussienne) concorde presque parfaitement pour une grande variété de conditions de rétrodiffusion, la pdf de l'amplitude correspondante tend à s'écarter fortement dans la plupart des cas. Basée sur cet écart, une distribution nouvelle est dérivée pour l'amplitude de l'interférogramme. Cette pdf, appelée distribution polynomiale ou distribution p, concorde beaucoup plus exactement avec les données réelles, en particulier pour un terrain composite extrêmement hétérogène. En se basant sur ces statistiques, on propose un système de détection entièrement automatique avec des taux de fausse alarme constants pour les cibles mobiles lentes. Tous les paramètres nécessaires pour déterminer les seuils de détection sont estimés à partir de l'échantillon de données. Il est démontré à l'aide d'une scène RAS réelle que ce détecteur est capable de détecter des véhicules se déplaant lentement dans un clutter de sol intense. Enfin, on aborde les aspects pratiques de la mise en application et de la stabilité numérique, puisqu 'un grand nombre des fonctions en cause se composent de séries de puissances indéfinies qui doivent être manipulées avec prudence.

P516111.PDF [Page: 7 of 69]

Executive summary

In air-to-ground radar surveillance it is desirable to be able to detect small moving targets such as tanks or wheeled vehicles within strong ground clutter. One possible way to achieve this is Along-Track SAR Interferometry (ATI). ATI exploits the difference in the echoes of two channels observing the same scene at different time. These channels are aligned in the flight direction of the platform. For stationary terrain the two channel signals are identical and can be canceled out (clutter suppression) by computing the phase difference, i.e. the interferogram, whereas the moving targets remain in the differential data. Precise knowledge of the interferogram's phase and amplitude statistics is crucial for the development of statistically based detector tests for distinguishing the moving targets from the clutter.

This report examines, theoretically, the statistics of the phase and magnitude of SAR interferograms towards the deployment of ATI for slow ground moving target detection. The theoretical results presented in this report were compared to real data acquired during an experiment conducted at Canadian Forces Base (CFB) Petawawa on July 14, 1999. While the known statistics of the interferogram's phase are shown to agree almost perfectly with the real data for a wide variety of backscatter conditions, the corresponding magnitude statistic deviates strongly in many cases. A novel distribution for the interferogram's magnitude is derived to overcome this problem. It is shown that this function matches the real data much more accurately, particularly for extremely heterogeneous composite terrain. Based on these new distributions, a constant false alarm rate (CFAR) detector scheme is proposed and its performance on real SAR scenes is demonstrated. This detector is fully autonomous, i.e. all needed parameters and thresholds are estimated from the sample data set. Further, some issues are addressed concerning the practical implementation, such as numerical stability.

While most statistical investigations on multi-channel SAR are either focused on across-track interferometry for the generation of digital elevation maps (DEM) or on polarimetry, this report deals with the problem of along-track interferometry for moving target detection. Since the introduced theoretical analysis is generally valid, the results are also useful for producing DEM's or for the polarimetric classification of targets. The detection thresholds based on the new statistic are much more accurate, i.e. they lead to significantly reduced false alarm rates, particularly for the operational case of extremely heterogeneous terrain. Great importance is attached to the practical applicability of the derived theoretical results, particularly with regard to the experimental MTI-mode of Radarsat2.

Christoph H. Gierull. 2001. Statistics of SAR Interferograms with Application to Moving Target Detection. DREO TR 2001-045. Defence Research Establishment Ottawa.

P516111.PDF [Page: 8 of 69]

Sommaire

En surveillance par radar air-sol, il est souhaitable d'être capable de détecter de petites cibles mobiles telles que des chars ou des véhicules à roues dans un clutter de sol intense. Un des moyens utilisés à cette fin est l'interférométrie RAS longitudinale (ATI). L'ATI met en valeur la différence entre les échos de deux canaux observant simultanément une même scène. Ces canaux sont alignés dans la direction de vol de la plate-forme. Pour le terrain stationnaire, les signaux des deux canaux sont identiques et peuvent être éliminés (suppression du clutter) au moyen du calcul du déphasage, c.-à-d. l'interférogramme, alors que les cibles mobiles demeurent dans les données différentielles. La connaissance exacte des statistiques de phase et d'amplitude de l'interférogramme est essentielle à l'élaboration d'essais de détection de cibles mobiles.

Le présent rapport examine théoriquement les statistiques de phase et d'amplitude d'interférogrammes RAS en vue de l'application de l'ATI à la détection de cibles terrestres mobiles lentes. Les résultats théoriques présentés dans ce rapport ont été comparés avec des données réelles acquises lors d'une expérience effectuée à la base des Forces canadiennes (BFC) Petawawa le 14 juillet 1999. Alors qu'il est démontré que les statistiques connues de la différence de phase de l'interférogramme concordent presque parfaitement avec les données réelles pour une grande variété de conditions de rétrodiffusion, les statistiques d'amplitude correspondantes s'écartent fortement dans bien des cas. Une distribution nouvelle de l'amplitude de l'interférogramme est dérivée pour régler ce problème. Il est démontré que cette fonction concorde beaucoup plus exactement avec les données réelles, en particulier pour un terrain composite extrêmement hétérogène. En se basant sur ces nouvelles distributions, on propose un système de détection de taux de fausse alarme constant (CFAR) et on fait la démonstration de ses performances sur des scènes RAS réelles. Ce détecteur est entièrement autonome: tous les paramètres et seuils nécessaires sont estimés à partir de l'échantillon de données. De plus, on aborde quelques questions ayant trait à la mise en application pratique, telle que la stabilité numérique.

Alors que la plupart des études statistiques du RAS à canaux multiples se concentrent soit sur l'interférométrie transversale pour la production de cartes altimétriques numériques (CAN), soit sur la polarimétrie, le présent rapport aborde le problème de l'interférométrie longitudinale en vue de la détection de cibles mobiles. Puisque l'analyse théorique présentée est généralement valide, les résultats sont également utiles pour produire des CAN ou pour la classification polarimétrique des cibles. Les seuils de détection basés sur les nouvelles statistiques sont beaucoup plus précis, c.-à-d. qu'ils donnent lieu à des taux de fausse alarme grandement réduits, en particulier dans le cas opérationnel d'un terrain

P516111.PDF [Page: 9 of 69]

extrêmement hétérogène. Une grande importance est accordée à l'applicabilité pratique des résultats théoriques dérivés, notamment à l'égard du mode MTI expérimental de Radarsat2.

Christoph H. Gierull. 2001. Statistiques d'interférogrammes RAS appliquées à la détection des cibles mobiles. DREO TR 2001-045. Centre pour la Recherche de la Défence Ottawa.

This page intentionally left blank.

P516111.PDF [Page: 11 of 69]

Table of contents

Abstract i

Résumé ii

Executive summary iii

Sommaire iv

Table of contents vii

List of figures ix

1. Introduction 1

1.1 Background 1

1.2 Real Data 2

2. Homogeneous (Gaussian) Clutter 5

2.1 Joint Probability Density Function of Magnitude and Phase 6

2.2 Marginal Probability Density Function of Phase 8

2.3 Marginal Probability Density Function of Magnitude 11

2.4 Conditional Probability Density Function of Phase for a fixed Magnitude 15

3. Heterogeneous (Non-Gaussian) Clutter 16

3.1 Exogenous Model 16

3.1.1 Compound One-Look Statistic 16

3.1.2 Extension to Multi-look Statistic 18

3.2 Novel Marginal Probability Density Function of Magnitude 21

4. CFAR Detector Scheme 26

4.1 Parameter Estimation 27

4.1.1 Coherence 27

P516111.PDF [Page: 12 of 69]

4.1.2 Effective Number of Looks 27

4.1.3 Model Parameter ν 33

4.2 Test Statistics 34

4.2.1 Small Resolution Cell Size 34

4.2.2 Large Resolution Cell Size 36

4.3 Results 37

5. Conclusions 40

References 41

Annexes viii

A Limit of the Conditional Variance of the Phase 44

B The Noncentral Inverse Chi-Square Distribution 45

C Probability Density Function of the Multilook Sample Covariance Matrix for Non-Gaussian Clutter 47

D Practical Implementations of the PDF's 48

D.1 Asymptotic Expansion of Modified Bessel Functions 48

D.2 Gauss' Hypergeometric Function for the Phase' PDF 48

P516111.PDF [Page: 13 of 69]

List of figures

1 HH polarized SAR image of CFB Petawawa, l6p7, July 14th, 1999. 3

2 Selected patches for the clutter analysis (the SAR image is upside-down with respect to Fig. 1).) 4

3 Theoretical joint probability density function of the interferogram's phase and magnitude. The number of looks is one. 7

4 Theoretical joint probability density function of the interferogram's phase and magnitude. The number of looks is ten. 8

5 One-look theoretical and empirical phase probability density function of patch one. 9

6 Ten-look theoretical and empirical phase probability density function of patch one. 10

7 One-look theoretical and empirical phase probability density function of patch 24. 10

8 Ten-look theoretical and empirical phase probability density function of patch 24. 11

9 One-look theoretical and empirical normalized magnitude probability density function for patch one. 13

10 Ten-look theoretical and empirical normalized magnitude probability density function for patch one. 13

11 One-look theoretical and empirical normalized magnitude probability density function for patch 24. 14

12 Ten-look theoretical and empirical normalized magnitude probability density function for patch 24. 14

13 One-look histogram of the real part of channel one for patch one. Normal distribution (dashed), $\mathcal{G}_C^0$-distribution (solid). 17

14 Schematic illustration of mean RCS; **(left)** uncorrelated from multilook cell to multilook cell but correlated with single-look cells,**(centre)** correlated with neighboring multillook cells and **(right)** uncorrelated from single-look cell to single-look cell. 19

P516111.PDF [Page: 14 of 69]

15 One-Look Pdf of real part of channel one, histogram (solid) and fitted Gaussian distribution (dashed). 20

16 Ten-Look Pdf of real part of channel one, histogram (solid) and fitted Gaussian distribution (dashed). 20

17 One-look density of p-distribution for different shape parameter. $\nu = 2.5$ (dotted), $\nu = 50$ (solid). Conventional interferogram magnitude for the Gaussian model (9) (dashed). 24

18 Ten-look density of p-distribution for different shape parameter. $\nu = 2.5$ (dotted), $\nu = 50$ (solid). Conventional interferogram magnitude for the Gaussian model (9) (dashed). 24

19 Ten-look p-density and empirical normalized magnitude density function of patch 1, $\nu = 7.6571$. Conventional interferogram magnitude for the Gaussian model (9) (dashed). 25

20 Ten-look p-density and empirical normalized magnitude density function of patch 24, $\nu = 17.1978$. Conventional interferogram magnitude for the Gaussian model (9) (dashed). 25

21 Flow-chart of the two-step ATI-MTI signal processing chain. 26

22 Window function of the interferometric processor. 28

23 Log-Likelihood function versus number of looks for patch 24. 30

24 Marginal probability density function of the phase of patch 24 for an effective number of looks $n = 3.4$. 31

25 Marginal probability density function of the phase of patch 24 for an effective number of looks $n = 4.49$. 32

26 Histogram of the Maximum-Likelihood estimation of n for simulated phase data along with the normal distribution given by the plotted expectation and variance. 32

27 Phase threshold for the moving target detector depending on the given false alarm probability. 34

28 Amplitude threshold for the moving target detector depending on the given false alarm probability. 35

P516111.PDF [Page: 15 of 69]

29 Histogram of the interferometric phase for the highway area along with the theoretical probability density function. 37

30 Histogram of the interferometric magnitude for the highway area along with the p-distribution (solid) and the original magnitude pdf (dashed). . . 38

31 SAR image of the Petawawa target area used for slow moving target detection. All marked detections correspond to $\alpha = 2.5 \cdot 10^{-5}$, whereas the circled target relates to $\alpha = 1 \cdot 10^{-6}$. The arrow indicates an undetected fast mover. 39

D.1 Error of direct-sum implementations of Gauss hypergeometric function versus coherence for integral number of looks. 50

D.2 Error of direct-sum implementations of Gauss hypergeometric function versus number of looks for different coherences. 50

1. Introduction

1.1 Background

In the past several years the statistics of the intensity and phase of multi-channel SAR imagery has been intensively studied. In polarimetry, the statistics help with the detection and discrimination of target signatures in a ground clutter background [5-7]. In another major application, the across-track SAR interferometry, the exact knowledge of the statistics is crucial in order to quantitatively analyse the influence of decorrelation on the phase and hence measure the achievable height accuracy, e.g. [8-10]. Although, these statistics are, in principle, directly applicable to the problem of moving target detection via along-track interferometry, no explicit study or investigation is known to the author.

In along-track interferometry, knowledge of the probability distribution of the phase difference will offer the possibility to derive a constant false alarm rate (CFAR) detector for moving targets. Previous derivations used the underlying assumption of jointly Gaussian-distributed data in each of the two images (see section 2). However, experimental data indicate large deviations from the consequent Rayleigh statistics, for instance over sea surface or urban areas. In such cases the observed distributions show longer tails and larger variance-to-expectation-ratios than predicted by the Gaussian distribution (spiky clutter).

Among many non-Gaussian statistics, the Weibull and K-distribution have proven particularly useful in characterizing the amplitude distribution of electromagnetic echoes from heterogeneous terrain, for instance, the sea surface [1]. The K -distribution results when the mean RCS of the individual scatterer is itself randomly distributed with a Chi-square distribution on spatial scales close to, or larger than, the spatial resolution [2]. Unfortunately, even the K-distribution sometimes fails to model extremely heterogeneous clutter such as that of urban areas. Moreover, when the area of interest is large compared to the size of the potential targets, e.g. large swathwidth, the scene might consists of composite landscape types, such as urban areas surrounded by forests and farmland. Furthermore, the modified Bessel functions often make the calculation of tests and thresholds a difficult and unstable numerical task, especially for large arguments that are typical for along-track interferometry with high coherence and large RCS (see section 2.3).

Analytical studies of the statistics of the multilook interferogram's phase and magnitude are very rare for non-Gaussian SAR image distributions. In this report, a recently proposed generalised distribution to describe the statistic of the

SAR image amplitude[1] will be applied to derive an analytical density function for the interferogram amplitude for extremely heterogeneous terrain. This family of distributions does not contain Bessel functions, yet results in density functions which have the same number of parameters as the K-distribution. This distribution arises when the SAR image amplitude (or mean RCS) can be modeled as the square root of an inverse Gaussian-distributed random variable [3].

1.2 Real Data

The theoretical results presented in this report were compared to real data acquired during an experiment conducted at Candian Forces Base (CFB) Petawawa on July 14, 1999. SAR GMTI data was acquired by the Environment Canada CV 580 C-band SAR configured in its along-track interferometer (ATI) mode. The surface component of the experiment provided GPS monitored, controlled moving targets for use in validating SAR GMTI, and video monitored targets of opportunity to provide a range of realistic vehicle target signatures and speeds. The controlled targets included a set of unobstructed, moving corner reflectors sited in terrain that has a low radar cross section. The entire experiment including several preliminary results is described in detail in [4]. Fig. 1 shows a SAR image of the test site. The urban component of CFB Petawawa is seen at the bottom left of the image. The experiment site, including Highway 17, occupies the upper left half of the image.

Several nearly homogeneous areas within line 7, pass 10, have been chosen to compare the theoretical probability function given in the following section with some real clutter data, see Fig. 2. Some different larger patches have been used for heterogeneous composite clutter. These patches include moving targets and are also used to demonstrate the detector performance in section 4.

[1]The so-called $\mathcal{G}^0$ distribution [3].

P516111.PDF [Page: 19 of 69]

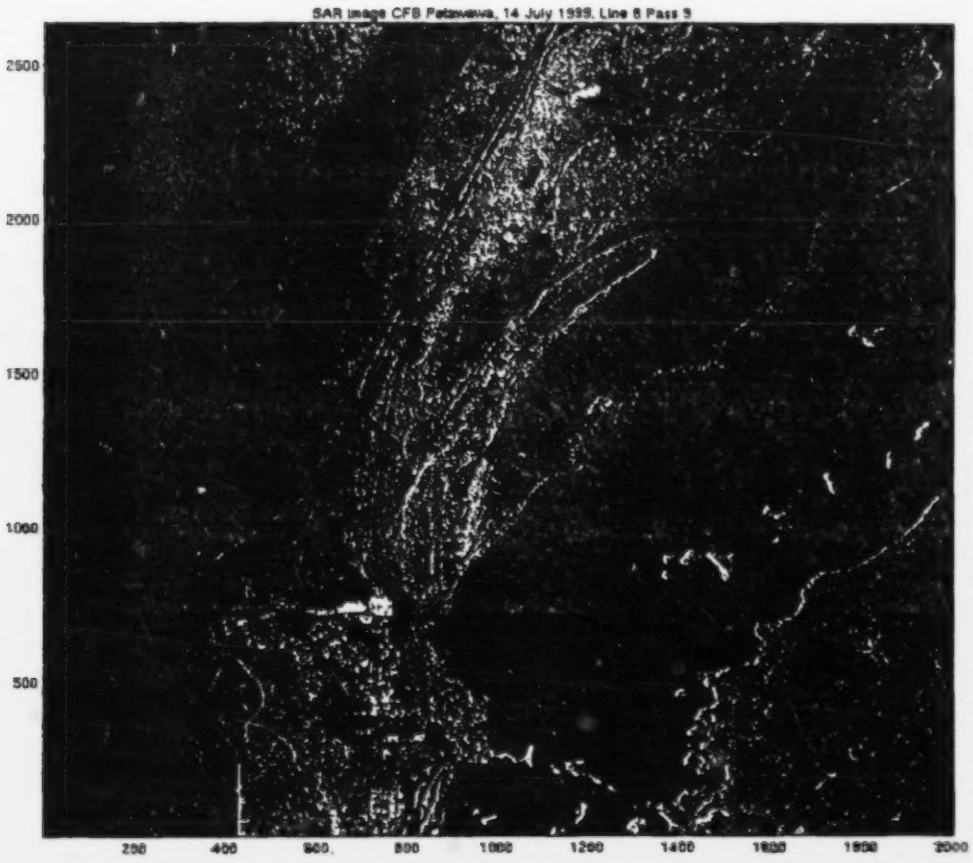

Figure 1 : *HH polarized SAR image of CFB Petawawa, l6p7, July 14th, 1999.*

P518111.PDF [Page: 20 of 69]

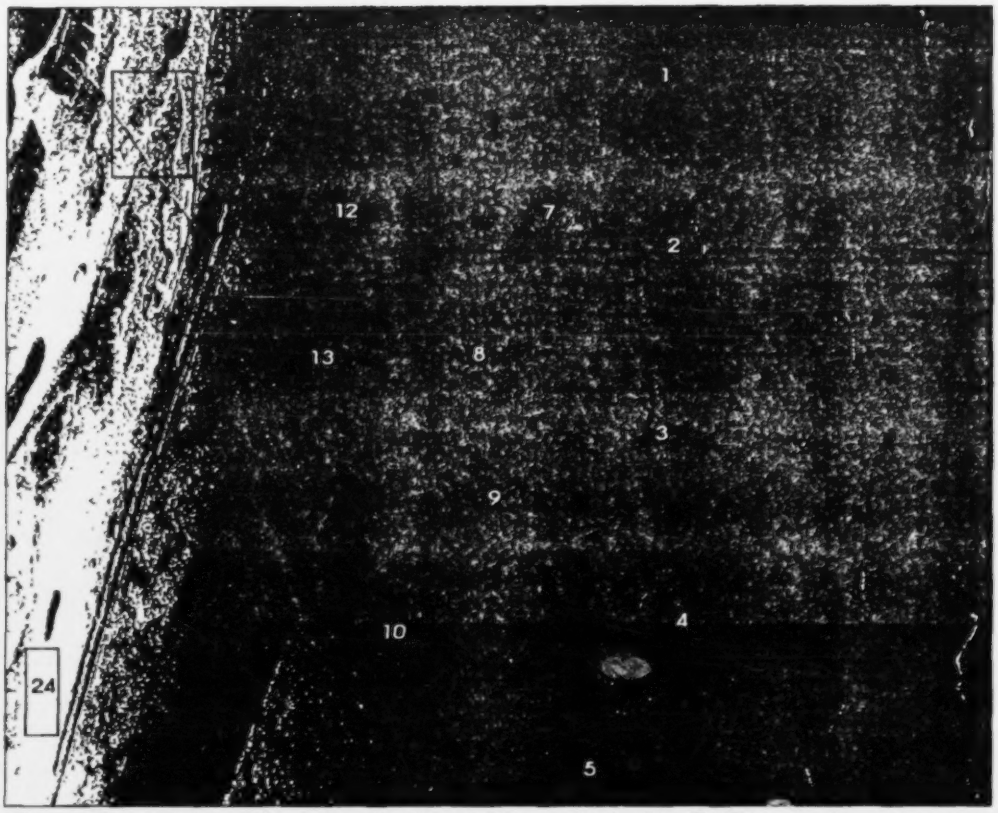

Figure 2 : *Selected patches for the clutter analysis (the SAR image is upside-down with respect to Fig. 1).)*

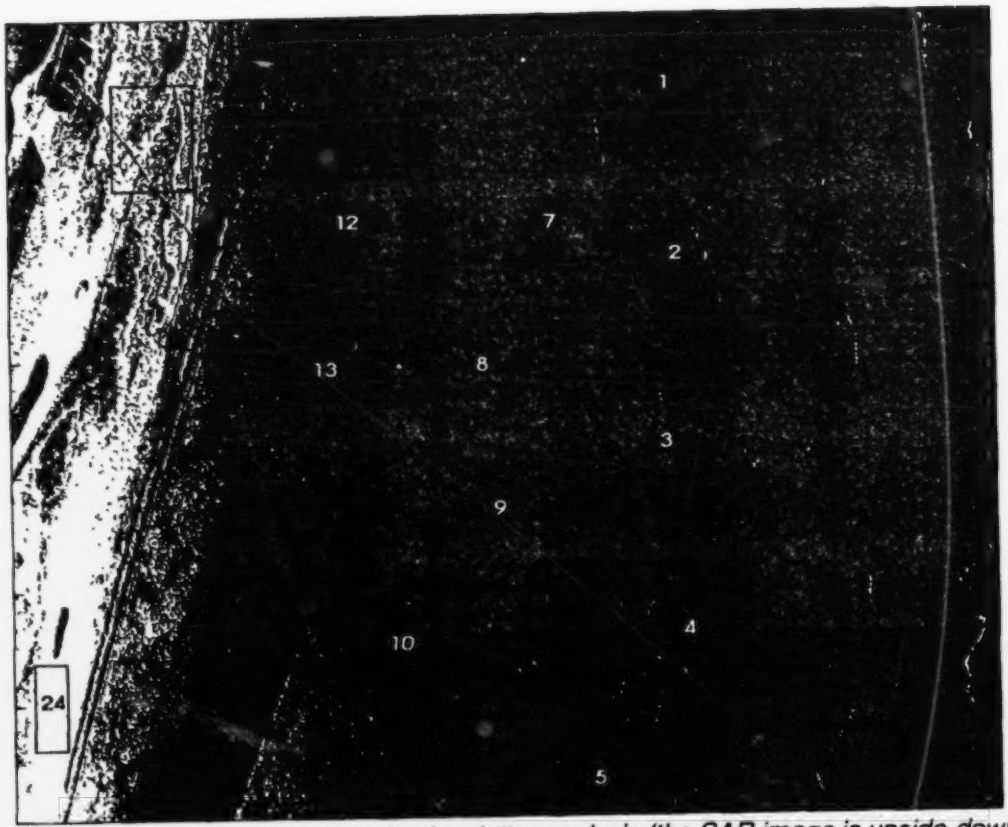

Figure 2 : *Selected patches for the clutter analysis (the SAR image is upside-down with respect to Fig. 1).)*

2. Homogeneous (Gaussian) Clutter

The amplitude of the clutter is often assumed to be Rayleigh-distributed, implying that the quadrature components of the received echoes are jointly Gaussian processes. This fact assumes a very rough (on the scale of the wavelength) but homogeneous amplitude backscatter, i.e. a constant mean radar cross section (RCS) σ across the imaged area. If this assumption is valid, the complex image can be regarded as resulting from the sum of statistically independent contributions from many randomly oriented elementary scatterers. The central limit theorem states that such a summation can be modeled as complex normal distribution regardless of the single backscatter distributions. This effect results in a granular pattern and is commonly denoted as speckle [5]. The assumption has been proven to be justified in most agricultural and natural areas, whereas it may not be warranted in more heterogeneous surfaces like urban areas or sea surfaces.

Let the zero-mean complex signals of N different channels define the vector $\underline{Z} = [Z_1, \cdots, Z_N]$. Under the assumptions mentioned above, $\underline{Z}$, with

$$Z_i = \sigma_i X_i \quad \forall \quad i = 1, \cdots, N \qquad \text{where} \quad \underline{X}_i \sim \mathcal{N}^{\mathbb{C}}(0,1), \tag{1}$$

can be modeled as a multivariate complex Gaussian random vector with density

$$f_{\underline{Z}}(\underline{z}) = \frac{1}{\pi^N \det(\mathbf{R})} \exp\left(-\underline{z}^H \mathbf{R}^{-1} \underline{z}\right),$$

where $\mathbf{R}$ denotes the covariance matrix $\mathbf{R} = \mathrm{E}\underline{Z}\underline{Z}^H$. The superscript H denotes complex conjugate transpose and $\det(\mathbf{R})$ the determinant of $\mathbf{R}$ [6]. In the case of interferometry usually only two channels are involved, i.e. the dimension of $\underline{Z}$ is chosen to be $N = 2$ from here onwards (without loss of generality) and the off-diagonal elements of the covariance matrix $\mathbf{R}$ correspond to the desired complex interferogram.

In order to reduce the speckle, polarimetric and interferometric data are frequently multilook processed. Multilook interferometric processing requires averaging several independent one-look interferograms. In other words several independent one-look sample covariance matrices are averaged. The n-look sample covariance matrix is given as

$$\hat{\mathbf{R}} = \frac{1}{n} \sum_{k=1}^{n} \underline{z}_k \underline{z}_k^H \tag{2}$$

where n is the number of looks and $\underline{z}_k$ the k-th one-look sample (also called snapshots). The sample covariance matrix is well-known to be complex Wishart-

distributed $\mathbf{A} = n\hat{\mathbf{R}} \sim \mathcal{W}_2^c(n, R)$ [6] with probability density

$$f_{\mathbf{A}}(\mathbf{A}) = \frac{\det(\mathbf{A})^{n-2}}{I_n(\mathbf{R})} \exp\left(-\mathrm{tr}\{\mathbf{R}^{-1}\mathbf{A}\}\right) \tag{3}$$

where $I_n(\mathbf{R}) = \pi\Gamma(n)\Gamma(n-1)|\mathbf{R}|^n$. Based on this density function, the multilook phase-difference and multilook amplitude have been derived in [7, 8].

2.1 Joint Probability Density Function of Magnitude and Phase

The joint probability $f_{\mathcal{E},\Psi}(\eta, \psi)$ of the multilook amplitude [2] and phase of the interferogram has been given as

$$f_{\mathcal{E},\Psi}(\eta, \psi) = \frac{2n^{n+1}\eta^n}{\pi\Gamma(n)(1-|\rho|^2)} \exp\left(\frac{2n\eta|\rho|\cos\psi}{1-|\rho|^2}\right) K_{n-1}\left(\frac{2n\eta}{1-|\rho|^2}\right) \tag{4}$$

where K_n is the modified Bessel function of order n [2, 7, 9].

The variable $|\rho|$ denotes the magnitude of the complex correlation coefficient of the two images. The complex correlation coefficient is one important parameter in characterizing the statistics. It is defined as

$$\rho = \frac{\mathrm{E}Z_1Z_2^*}{\sqrt{\mathrm{E}|Z_1|^2\,\mathrm{E}|Z_2|^2}} = \frac{\mathrm{E}Z_1Z_2^*}{\sigma_1\sigma_2} = |\rho|\exp j\theta \tag{5}$$

with E denoting the expectation operator. The magnitude of the complex correlation coefficient will be referred to as coherence in the following for simplification of notation. Cross-channel correlation is a potential source of information in different areas of remote sensing. It is a composite measure of all effects which lead to any decorrelation of the signals, for example, temporal decorrelation due to surface or backscatter changes added to the unavoidable receiver or sensor noise. In across-track interferometry, for instance, the coherence is computed to select areas in which accurate digital elevation models (DEM) can be generated. The precision of such DEM's are highly dependent on the coherence magnitude, particularly for repeat-pass interferometry, e.g. [10]. The coherence might also be used to determine the signal-to-noise ratio for a given radar system. Typical values for solid surfaces in single-pass across-track interferometry as well as for along track interferometry are between 0.94 and 0.99. The value is smaller for water surfaces at about 0.8. The statistical properties of the Maximum-Likelihood Estimator of the coherence based on (5) are given

[2] Normalized to the product of the power of the two single channels $\sigma_1\sigma_2$

in [11]. Herein, it is shown analytically that this commonly used estimator is highly biased under low coherence conditions when calculated with only a small number of samples (see section 4.1.1).

Two examples of the joint density function of (4) are plotted in Fig. 3 and 4 for $n = 1$ and $n = 10$, respectively. The mutual coherence between the looks was chosen to be $|\rho| = 0.981$. Fig. 3 shows the typical behavior of the phase fluctuation (variance), large for small clutter amplitudes and strongly decreasing for larger magnitudes. Increasing the number of independent looks clearly leads to speckle reduction and hence smaller variance even for moderate interferogram magnitudes.

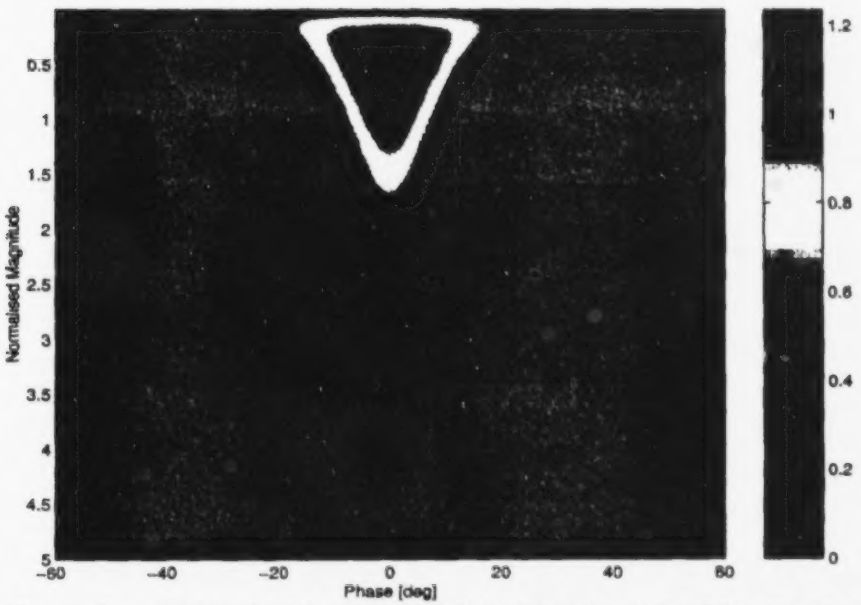

Figure 3 : *Theoretical joint probability density function of the interferogram's phase and magnitude. The number of looks is one.*

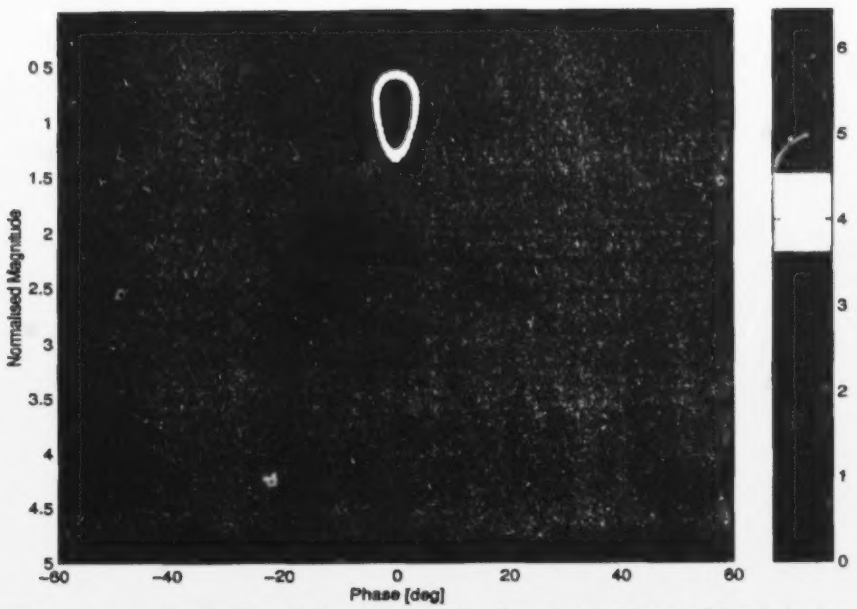

Figure 4 : *Theoretical joint probability density function of the interferogram's phase and magnitude. The number of looks is ten.*

2.2 Marginal Probability Density Function of Phase

The multilook phase difference between the two channels is obtained by

$$\Psi = \arg\left(\frac{1}{n}\sum_{k=1}^{n} z_1(k) z_2(k)^*\right). \tag{6}$$

Ψ is the argument of the off-diagonal term in the multilook sample covariance matrix $\hat{\mathbf{R}}$.

Integrating (4) over the magnitude variable η leads to the marginal multilook density function for the phase

$$f_\Psi(\psi) = \frac{\Gamma(n+1/2)\left(1-|\rho|^2\right)^n \beta}{2\sqrt{(\pi)}\Gamma(n)\left(1-\beta^2\right)^{n+1/2}} + \frac{\left(1-|\rho|^2\right)^n}{2\pi}\, {}_2F_1(n,1;1/2;\beta^2) \tag{7}$$

for $-\pi < \psi \leq \pi$, where $\beta = |\rho|\cos\psi$. Herein, ${}_2F_1(\cdot)$ denotes the Gauss hypergeometric function, see e g. [12]. The pdf of (7) depends only on the number of looks and the magnitude of the complex correlation coefficient. The peak of the distribution is located at $\psi = \theta$. For the application of along-track interferometry

the peak should be centered around zero, assuming the data are accurately calibrated. It can be shown that the phase is uniformly distributed when $|\rho| = 0$ and becomes a Dirac delta function when $|\rho| = 1$. It is also evident that multilook processing improves the phase accuracy, i.e. the variance of the phase decreases for a larger number of looks [13, 7].

Fig. 5-8 show representative results of the empirical phase distribution for different numbers of looks and different surface types. For convenience, the peaks of the histograms are normalized to one and the corresponding density functions scaled accordingly. Patch 24 is mainly grass, and patch one is widely covered with jackpines. The coherence has been estimated according to (28). These examples demonstrate on one hand the almost perfect agreement of the theoretical and empirical results, and on the other hand, that the phase statistic is mainly independent of the clutter or surface type. This observed property of the phase statistic strongly supports other, mainly polarimetric, studies that have reported identical results [7, 2]. An explanation will be given at the end of the following section.

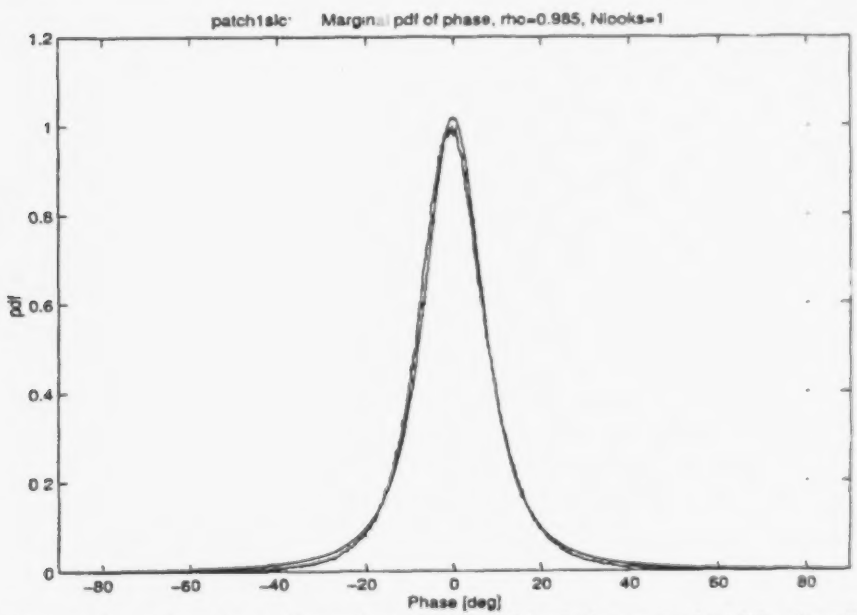

Figure 5 : *One-look theoretical and empirical phase probability density function of patch one.*

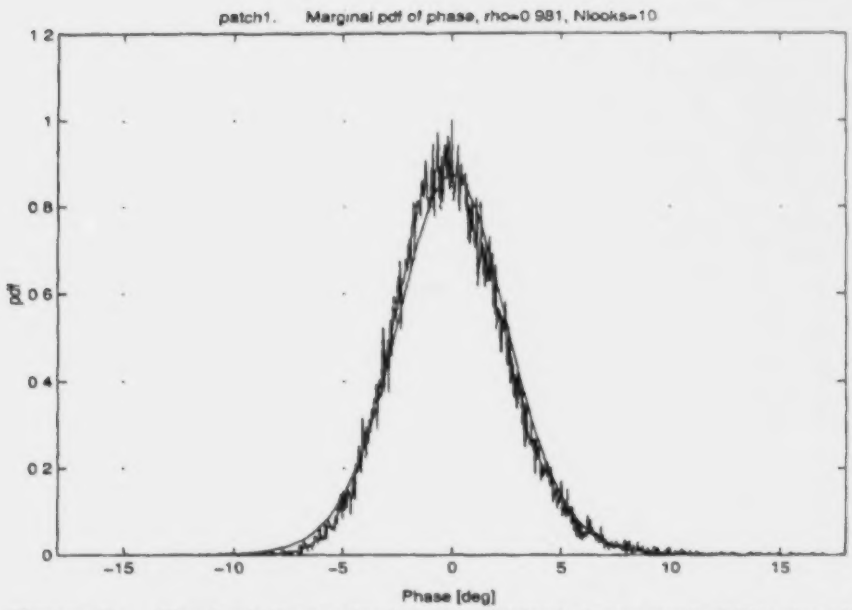

Figure 6 : *Ten-look theoretical and empirical phase probability density function of patch one.*

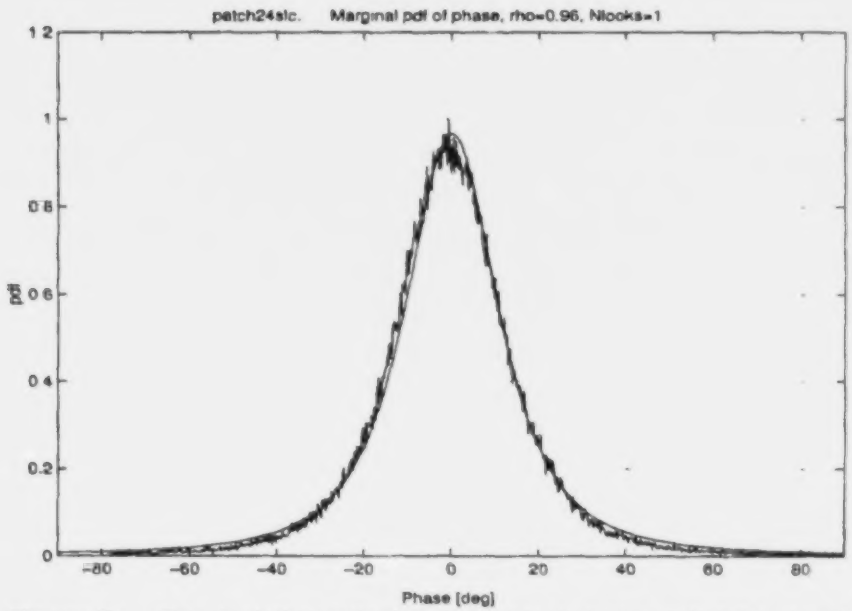

Figure 7 : *One-look theoretical and empirical phase probability density function of patch 24.*

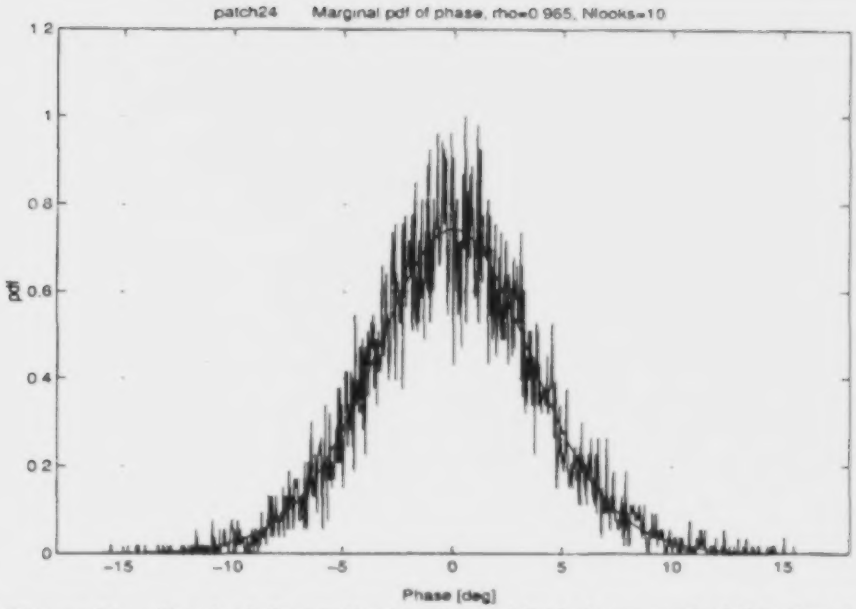

Figure 8 : *Ten-look theoretical and empirical phase probability density function of patch 24.*

2.3 Marginal Probability Density Function of Magnitude

The magnitude of the product of z_1 and z_2^* represents the magnitude of the interferogram. It can also be used as a measure for detecting moving targets since they often have a higher radar cross section than their surrounding stationary environment. The normalized multilook interferogram magnitude is defined as

$$\mathcal{E} = \frac{\left|\frac{1}{n}\sum_{k=1}^{n} z_1(k) z_2(k)^*\right|}{\sqrt{\mathrm{E}|z_1|^2 \ \mathrm{E}|z_2|^2}} = \frac{1}{n}\frac{\left|\sum_{k=1}^{n} z_1(k) z_2(k)^*\right|}{\sigma_1 \sigma_2}. \tag{8}$$

It should be pointed out, that the normalization in along-track interferometry is very often performed by replacing the denominator in (8) with the sample mean value taken over L pixels of the (n-look) interferogram amplitudes, i.e.

$$\bar{\mathcal{E}} = \frac{1}{L}\sum_{l=1}^{L} \mathcal{E}_l,$$

where $\mathcal{E}_l$ is given by the numerator of (8). For coherence values close to one, the substitution is a valid approximation because

$$\mathrm{E}\bar{\mathcal{E}} = \rho\sigma_1\sigma_2 \cong \sigma_1\sigma_2 \qquad \text{if} \quad \rho \cong 1.$$

The pdf of the amplitude η, derived by integrating (4) with respect to the phase ψ, is given as

$$f_{\mathcal{E}}(\eta) = \frac{4n^{n+1}\eta^n}{\Gamma(n)\,(1-|\rho|^2)} I_0\left(\frac{2n\eta|\rho|}{1-|\rho|^2}\right) K_{n-1}\left(\frac{2n\eta}{1-|\rho|^2}\right) \tag{9}$$

where I_0 and K_{n-1} are modified Bessel functions of order zero and $n-1$, respectively [7]. The variance of $\mathcal{E}$ again decreases for larger number of looks. Fig. 9-12 show the corresponding empirical and theoretical pdf's for the multilook magnitudes. The plots show that the magnitude distribution varies with the surface type. For patch 24 the Gaussian assumption for the backscatter distribution seems valid, whereas for patch one it does not.

Since the term $n\eta$ can be large for many practical cases (and the Bessel function $K(\cdot)$ tends to infinity rapidly), the accuracy of a direct computation of (9) can be poor, especially with a limited precision data format. In the following, one possible way to overcome this problem is introduced. An asymptotic expansion of the product of the two Bessel functions, see (D.1) and (D.2), in (9) can be written as

$$\begin{aligned} I_0(c|\rho|)\,K_{n-1}(c) &\cong \frac{\exp(-(1-|\rho|)c)}{2\sqrt{|\rho|c}} \\ &\cdot\left(\sum_{k=0}^{K}(-1)^k\frac{\Gamma\left(k+\frac{1}{2}\right)}{\Gamma(k+1)\Gamma\left(\frac{1}{2}-k\right)}\frac{1}{(2|\rho|c)^k}\right)\left(\sum_{k=0}^{K}\frac{\Gamma\left(n+k-\frac{1}{2}\right)}{\Gamma(k+1)\Gamma\left(n-\frac{1}{2}-k\right)}\frac{1}{(2c)^k}\right) \\ &= \frac{\exp(-(1-|\rho|)c)}{2\sqrt{|\rho|}} \\ &\cdot\sum_{k=0}^{K}\sum_{m=0}^{K}\frac{(-1)^k\Gamma\left(k+\frac{1}{2}\right)\Gamma^{-1}(k+1)\Gamma\left(n+m-\frac{1}{2}\right)}{\Gamma\left(\frac{1}{2}-k\right)\Gamma(m+1)\Gamma\left(n-m-\frac{1}{2}\right)}\frac{1}{2^{k+m}|\rho|^k c^{k+m+1}} \end{aligned} \tag{10}$$

with $c = 2n\eta/(1-|\rho|^2)$. Substituting the product-expansion of (10) into (9) then yields

$$\begin{aligned} f_{\mathcal{E}}(\eta) = \frac{1}{\Gamma(n)}\exp\left(-\frac{2n\eta}{(1+|\rho|)}\right) \\ \cdot\sum_{k=0}^{K}\sum_{m=0}^{K}\left(\frac{(-1)^k\Gamma\left(k+\frac{1}{2}\right)\Gamma^{-1}(k+1)\Gamma\left(n+m-\frac{1}{2}\right)}{\Gamma\left(\frac{1}{2}-k\right)\Gamma(m+1)\Gamma\left(n-m-\frac{1}{2}\right)}\right. \\ \left.\cdot\frac{|\rho|^{-(k+1/2)}\left(1-|\rho|^2\right)^{k+m}}{2^{2(k+m)}n^{k+m-n}\eta^{k+m-n+1}}\right). \end{aligned} \tag{11}$$

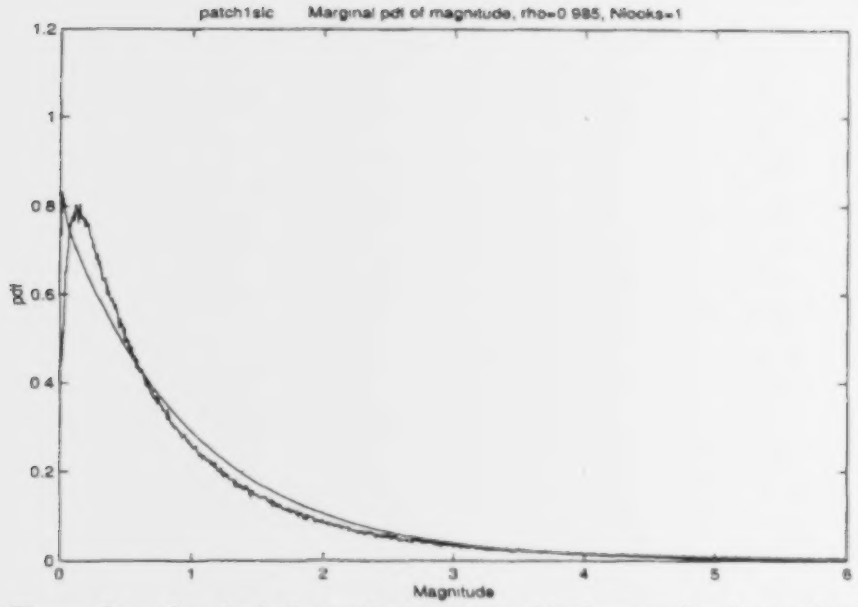

Figure 9 : *One-look theoretical and empirical normalized magnitude probability density function for patch one.*

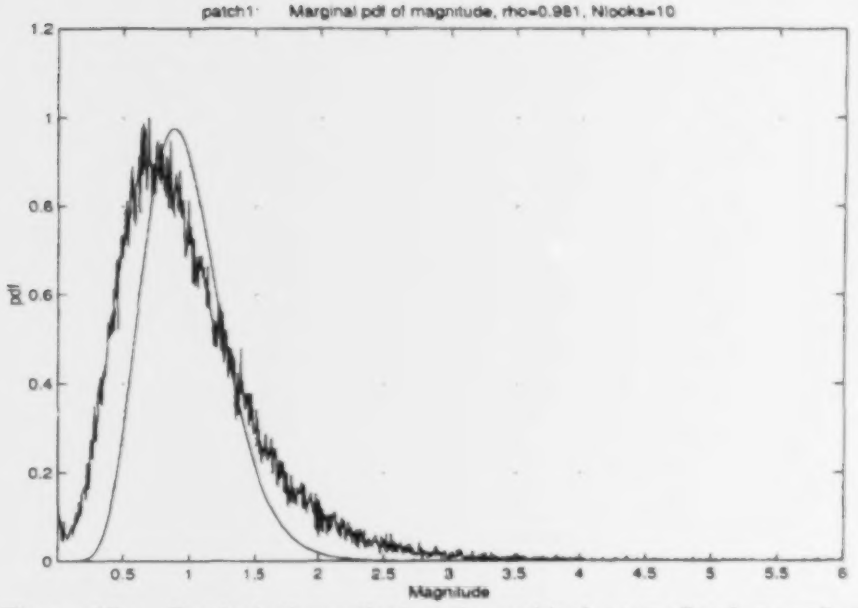

Figure 10 : *Ten-look theoretical and empirical normalized magnitude probability density function for patch one.*

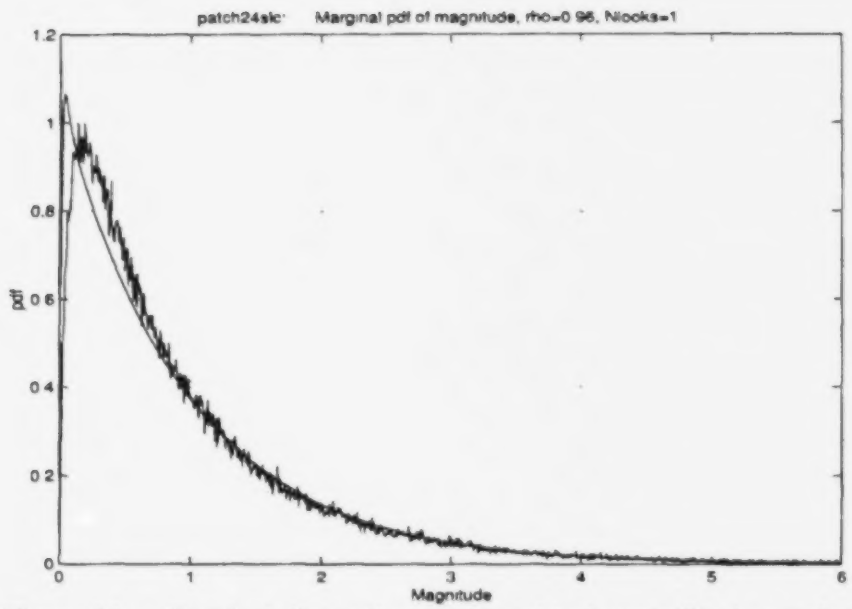

Figure 11 : *One-look theoretical and empirical normalized magnitude probability density function for patch 24.*

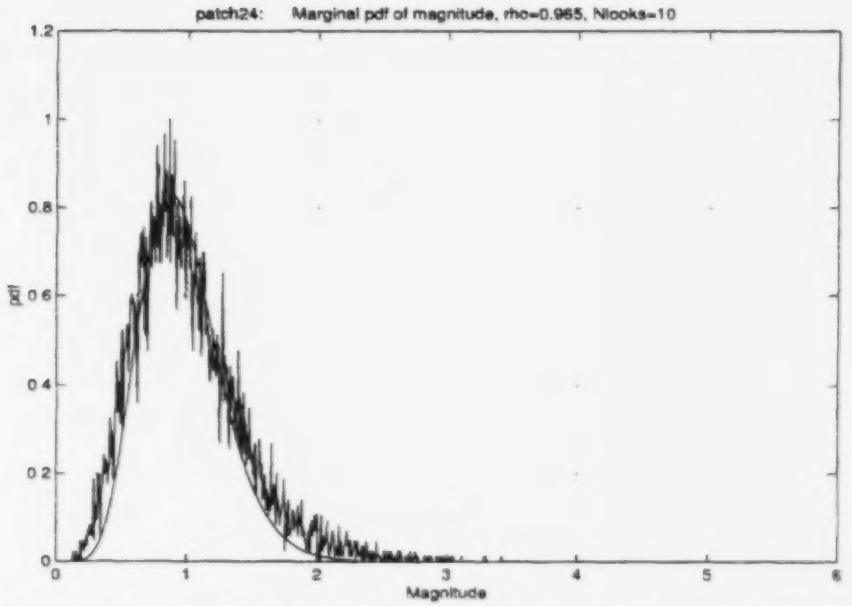

Figure 12 : *Ten-look theoretical and empirical normalized magnitude probability density function for patch 24.*

2.4 Conditional Probability Density Function of Phase for a fixed Magnitude

For future moving target detectors it might be advantageous to work with limited ranges for the interesting parameters. It can, for instance, be interesting to look at phase differences for some specific magnitude values. In order to develop such a detector, the so-called conditional pdf of the phase for a fixed magnitude has to be known. This conditional density $f_{\Psi|\mathcal{E}=\eta}(\psi|\eta)$ is defined as [14]:

$$f_{\Psi|\mathcal{E}=\eta}(\psi|\eta) = \frac{f_{\mathcal{E},\Psi}(\eta,\psi)}{f_{\mathcal{E}}(\eta)}, \tag{12}$$

assuming that $f_{\mathcal{E}}(\eta) > 0$. Inserting (4) and (9) into (12) yields

$$f_{\Psi|\mathcal{E}=\eta}(\psi|\eta) = \frac{1}{2\pi}\frac{\exp\left(2n\eta|\rho|\cos\psi/(1-|\rho|^2)\right)}{I_0\left(2n\eta|\rho|/(1-|\rho|^2)\right)}. \tag{13}$$

Again, the term $n\eta$ can be large and the accuracy of (13) might be limited. Using the Annex D.1, (13) can be written as

$$f_{\Psi|\mathcal{E}=\eta}(\psi|\eta) = \sqrt{\frac{n\eta|\rho|}{\pi(1-|\rho|^2)}}\exp\left(\frac{2n\eta|\rho|}{1-|\rho|^2}(\cos\psi-1)\right) \tag{14}$$
$$\Big/\left(\sum_{k=0}^{K}(-1)^k\frac{\Gamma\left(k+\frac{1}{2}\right)}{\Gamma(k+1)\Gamma\left(\frac{1}{2}-k\right)}\frac{1}{(4n|\rho|\eta/(1-|\rho|^2))^k}\right).$$

Further, in Annex A it is shown that the conditional variance tends to zero as the normalized magnitude tends to infinity, for any coherence value greater than zero. In other words, the conditional phase pdf (for fixed normalized magnitude) degenerates towards a Dirac delta function for larger magnitudes even if the two channels remain partly decorrelated. This property is important in cases where the underlying decorrelation effect is multiplicative in nature[3]. The impact of the additive noise on the signal decorrelation vanishes when the signal-to-noise ratio tends to infinity, i.e. the clutter magnitude tends to infinity and hence $|\rho|$ tends to one. In the case of multiplicative phase noise, for instance caused by oscillator jitter [15], this impact will not disappear and $|\rho|$ will converge to a constant value less than one.

[3]In contrast to the usual additive receiver noise

3. Heterogeneous (Non-Gaussian) Clutter

3.1 Exogenous Model

3.1.1 Compound One-Look Statistic

Experimental data amplitudes indicate large deviations from the Rayleigh-amplitude distribution, especially for heterogeneous terrain. In such cases the histograms show larger tails, i.e. a higher probability of larger SAR image amplitudes. It has become clear that a single amplitude distribution cannot accommodate all of the different scenarios. Instead, a class or family of distributions has to be considered, where the Rayleigh distribution must be a member. Among such, the Weibull and K-distribution have received a great deal of attention in the literature, e.g. [3],[16]. These distributions result from a compound (often called multiplicative) model for the clutter and have been proven to fit a wide range of experimental data well. Herein, it is assumed that under certain conditions [17] the one-look SAR returns can be modeled as a product of Gaussian speckle and an independent modulating random variable A (rather than a constant σ, see (1))

$$Z_i = AX_i \quad \forall \quad i = 1, \cdots, N \qquad \text{where} \quad \underline{X}_i \sim \mathcal{N}^{\mathbb{C}}(0,1). \qquad (15)$$

For the one-look K-distribution, the random variable A has a chi-square distribution [1] and for the Weibull distribution its density can be expressed in terms of Meijers G functions [16]. Even the K-distribution sometimes fails to model extremely heterogeneous clutter such as urban areas or areas of interest that are large compared to the size of the potential targets, i.e. the scene is so large that it consists of different landscape types. The generalization from a random variable A to a stochastic process $A(t)$ with certain correlation properties is investigated in [16]. The classical K- and Weibull-distributions have been extended by Frery et. al. [3] who proposed a square root of a generalized inverse Gaussian distribution for the modulating random variable A. It has been shown that the Rayleigh and also the K-distribution are special cases of this approach.

Fig. 13 demonstrates the failure of the Gaussian assumption for heterogeneous terrain. Here, the histogram of the real part or in-quadrature component of channel one is plotted along with two theoretical densities. The dashed one represents the fitted Gaussian distribution and the

solid one the so-called $\mathcal{G}_C^0$-distribution [3] with density

$$f_A(a) = \frac{\Gamma(\nu + 1/2)\gamma^\nu}{\sqrt{\pi}\Gamma(\nu)} \frac{1}{(a^2+\gamma)^{\nu+1/2}}. \tag{16}$$

The shape parameters ν and γ are estimated from the same dataset. It is evident that this recently proposed density matches the empirical data much better[4] than the Gaussian distribution which is significantly mismatched.

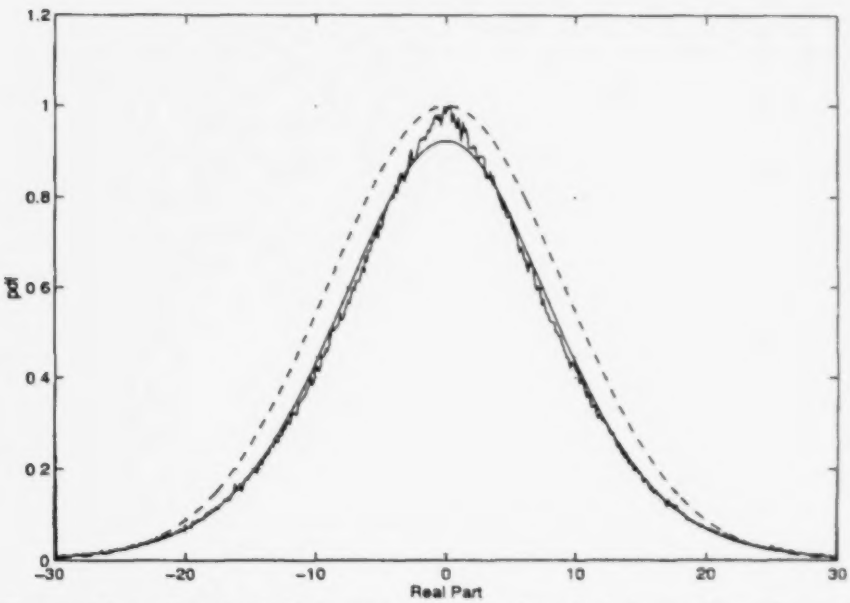

Figure 13 : *One-look histogram of the real part of channel one for patch one. Normal distribution (dashed), $\mathcal{G}_C^0$-distribution (solid).*

The proposed density in (16) does not involve modified Bessel functions unlike the K-distribution. The calculation of tests and thresholds for the K-distribution is often difficult and numerically unstable, especially for large arguments. Large arguments of the Bessel functions are typical for along-track interferometry with high coherence and backscatter RCS (compare also section 2.3).

[4]Except for a small area around zero. This is not crucial because the main interest lies in the shape of the tails in order to determine detector thresholds

3.1.2 Extension to Multi-look Statistic

If the one-look multiplicative model in (15) holds, it is evident that the ratios between channel amplitudes (commonly used in SAR polarimetry) as well as phase differences have exactly the same distribution as those derived for Gaussian data. This is due to the independent nature of the modulation or fluctuation of the random variable A in the compound model. The random variable A cancels out when the ratio or the phase is calculated.

For the SAR image amplitude, the K-distribution has been extended to the multilook case [18] and was shown to work well for sea-ice returns. Since the key assumption in this derivation is of major importance to the understanding of the physics behind the model and is also used in this report, it will be reviewed and summarized in the following. A large portion of the description and explanation is borrowed from Joughin et. al. [2].

Let the area of interest be divided into a certain number of multi-look resolution (or spatial) cells. An n-look cell consists of n one-look cells with sizes that are determined by system parameters such as bandwidth and processor parameters such as processed Doppler bandwidth and platform velocity. The situation is illustrated in Fig. 14. Herein, thick lines delimit multilook cells and thin lines delimit single-look cells. The mean RCS is qualitatively represented by the pattern of the squares.

Following the model (15), the received quadrature components X from each channel are normal-distributed with variance proportional to the underlying j-th single-look radar cross section A_j. This "local" RCS is assumed to be a random variable itself. Again, the choice of a chi-square distribution for A_j leads to a K-distribution of the SAR image intensity distribution.

Consider an n-look covariance matrix that is the average of single-look matrices given in (2) and substitute Z_j by (15), we get

$$\hat{\mathbf{R}}_n = \frac{1}{n}\sum_{j=1}^{n} A_j^2 \underline{X}_j \underline{X}_j^H. \tag{17}$$

By assuming that the backscatter fluctuation occurs on a scale greater than or equal to the size of the multilook cell (Fig. 14 left and centre), the single cell random variable A_j will effectively be all identical $A_j \equiv A$ within the n-look cell, though it may vary between neighboring

multilook cells. Hence, the random variable A can be factored out of the sum

$$\hat{\mathbf{R}}_n = \frac{A^2}{n} \sum_{j=1}^{n} \underline{X}_j \underline{X}_j^H = A^2 \hat{\mathbf{R}} \tag{18}$$

and the multiplier A^2 still cancels out when the phase (or any amplitude ratio) is calculated. The statistics of this ratio are identical to those of a homogeneous terrain (Gaussian assumption). The almost perfect agreement of theoretical and empirical marginal phase densities for different numbers of looks even for patch one in Fig. 5 and 6 validates this assumption.

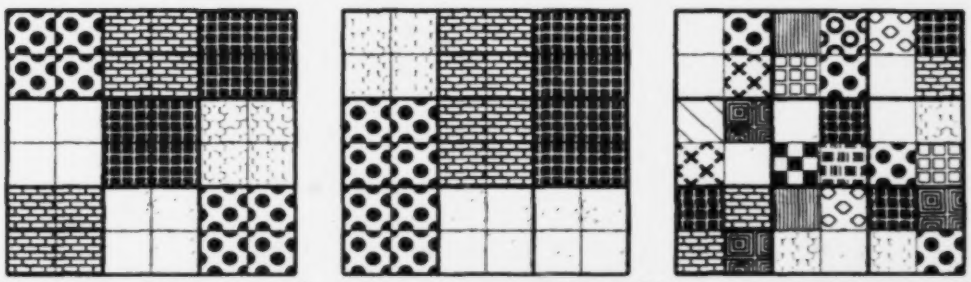

Figure 14 : *Schematic illustration of mean RCS;* **(left)** *uncorrelated from multilook cell to multilook cell but correlated with single-look cells,***(centre)** *correlated with neighboring multillook cells and* **(right)** *uncorrelated from single-look cell to single-look cell.*

Cross section fluctuations on scales smaller than the multilook cell size do not cancel out because A_j^2 is not constant across the n-look cell. Nonetheless, the summation of independent random variables with finite variance approaches a normal distribution as n increases, as does the corresponding summation in the case of the Gaussian assumption. The validity of this assumption is supported by the results in Fig. 15 and 16, in which the histogram of the real part of channel one is compared to a fitted Gaussian model for different number of looks. The standard deviations between the two curves are calculated and the much smaller value for ten looks indicates that the histogram indeed tends towards a Gaussian distribution as n increases. This suggests that the form of the multilook phase difference distribution in (7) from the homogeneous model may represent observations well for a sufficiently large number of looks, although shape parameters estimated from the data itself may differ from the true underlying covariance matrix.

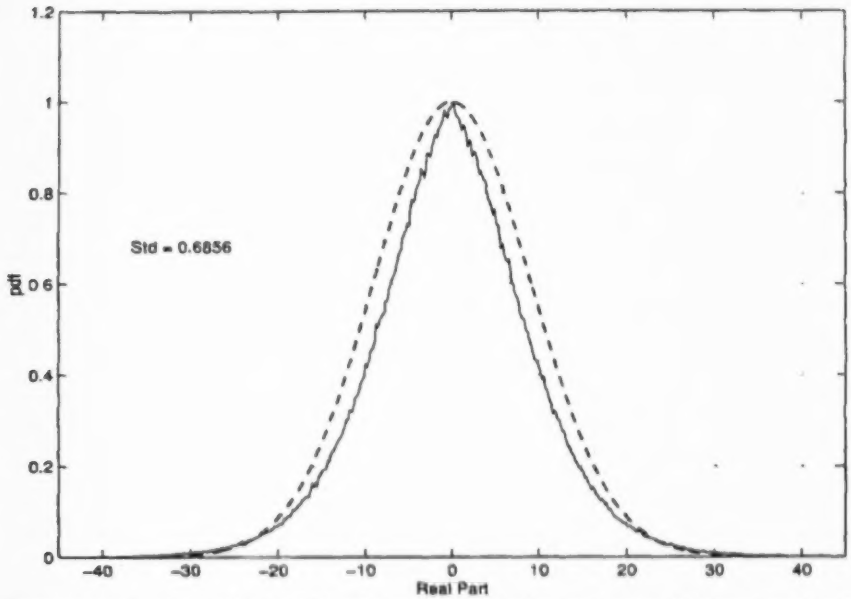

Figure 15 : *One-Look Pdf of real part of channel one, histogram (solid) and fitted Gaussian distribution (dashed).*

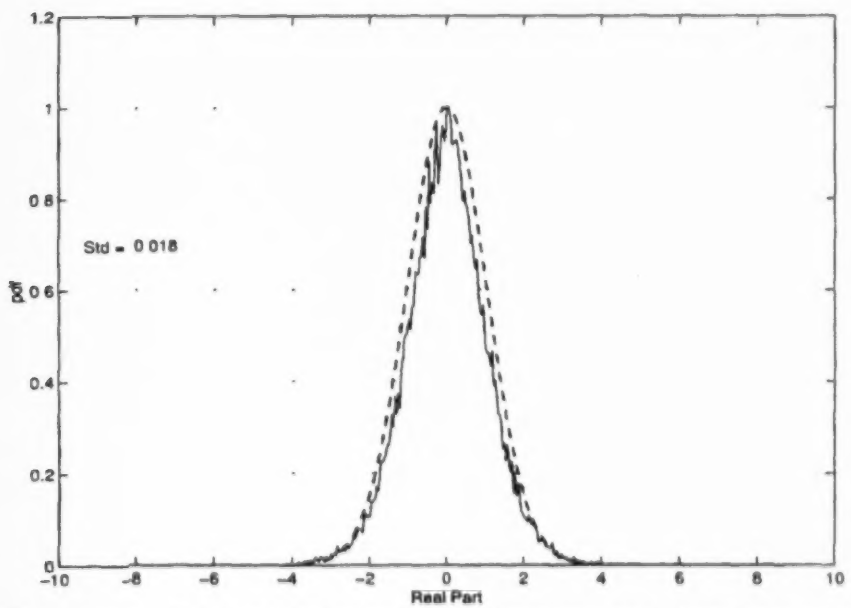

Figure 16 : *Ten-Look Pdf of real part of channel one, histogram (solid) and fitted Gaussian distribution (dashed).*

3.2 Novel Marginal Probability Density Function of Magnitude

Even though the multilook phase difference distribution has been retained unchanged, the interferogram's multilook magnitude differs from the Gaussian assumption case because A^2 in (18) does not cancel out. This can clearly be seen in the disagreement of histogram and theoretical pdf in Figs. 9, 10 and 13. In this section, a new analytical multilook density function for the magnitude will be derived and compared with observations.

Frery et. al. [3] proposed a reciprocal of the square root of a Gamma distribution (or generalized inverse Rayleigh distribution) as a statistic for A to characterize highly heterogeneous clutter. It is shown in Annex B that the square of A is then central inverse chi-square distributed with density (B.5). Using this distribution for A^2, a new closed form multilook density function for the modified sample covariance matrix in (18) has been calculated in Annex C:

$$f_{\hat{\mathbf{R}}_n}(\hat{\mathbf{R}}_n) = \frac{\mu^{\nu}\det(\hat{\mathbf{R}}_n)^{n-m}}{I_m(\mathbf{R})\Gamma(\nu)}\left(\frac{1}{\mu+\operatorname{tr}\{\mathbf{R}^{-1}\hat{\mathbf{R}}_n\}}\right)^{n+\nu-m+1}$$

where $I_m(\mathbf{R}) = \pi^{m(m-1)/2}\Gamma(n)\cdots\Gamma(n-m+1)\det(\mathbf{R})^n$.

Since all elements of the sample covariance matrix are multiplied by the same random variable, the modified interferogram magnitude Z is given by

$$Z = A^2\mathcal{E} := w\mathcal{E}, \tag{19}$$

with $w := A^2$, compare also (8). Using (C.2) in Annex C, the pdf of Z can be written as

$$\begin{aligned} f_Z(\zeta) &= \int_0^{\infty}\frac{1}{w}f_W(w)f_{\mathcal{E}}\left(\frac{\zeta}{w}\right)dw \\ &= \beta\int_0^{\infty}\left(\frac{1}{w}\right)^{n+\nu+2}\exp\left(-\frac{\mu}{w}\right)I_0\left(\frac{|\rho|\kappa}{w}\right)K_{n-1}\left(\frac{\kappa}{w}\right)dw \end{aligned} \tag{20}$$

where

$$\beta = \frac{4n^{n+1}\zeta^n\mu^{\nu}}{\Gamma(n)\Gamma(\nu)(1-|\rho|^2)} \qquad \text{and} \qquad \kappa = \frac{2n}{1-|\rho|^2}\zeta.$$

Substituting the integrand $t = 1/w$ and inserting the expansion (10) for the product of two Bessel functions leads to

$$\begin{aligned} f_Z(\zeta) &\cong \beta\sum_{k=0}^{K}\sum_{m=0}^{K}g_{m,k}\int_0^{\infty}t^{n+\nu-k-m-1}e^{[(|\rho|-1)\kappa-\mu]t}dt \\ &= \beta\sum_{k=0}^{K}\sum_{m=0}^{K}g_{m,k}\frac{\Gamma(n+\nu-k-m)}{(\mu-(|\rho|-1)\kappa)^{n+\nu-k-m}} \end{aligned} \tag{21}$$

with

$$g_{m,k} = \frac{(-1)^k \Gamma\left(k+\frac{1}{2}\right) \Gamma^{-1}(k+1) \Gamma\left(n+m-\frac{1}{2}\right)}{\Gamma\left(\frac{1}{2}-k\right) \Gamma(m+1) \Gamma\left(n-m-\frac{1}{2}\right)} \frac{1}{2^{k+m+1} |\rho|^{k+1/2} \kappa^{k+m+1}}.$$

Inserting $\kappa = 2n\zeta/(1-|\rho|^2)$ into (21) yields after some transformations

$$f_Z(\zeta) = \frac{n^n \mu^\nu \left(1-|\rho|^2\right)^{\nu+n}}{\Gamma(n)\Gamma(\nu)} \frac{\zeta^{n-1}}{\left((1-|\rho|^2)\mu - 2n(|\rho|-1)\zeta\right)^{n+\nu}}$$
$$\cdot \sum_{k=0}^{K} \sum_{m=0}^{K} \left(\frac{(-1)^k \Gamma\left(k+\frac{1}{2}\right)}{\Gamma(k+1)\Gamma\left(\frac{1}{2}-k\right)} \frac{\Gamma\left(n+m-\frac{1}{2}\right)\Gamma(n+\nu-k-m)}{\Gamma(m+1)\Gamma\left(n-m-\frac{1}{2}\right)|\rho|^{k+1/2}} \right.$$
$$\left. \cdot \left(\frac{\left(1-|\rho|^2\right)\mu - 2n(|\rho|-1)\zeta}{4n\zeta} \right)^{k+m} \right). \tag{22}$$

It can be numerically shown that the double sum in (22) can be well approximated by a constant value k over the entire range $\zeta \in \mathbb{R}_+$. Hence,

$$f_Z(\zeta) \cong k \frac{n^n}{\Gamma(n)\Gamma(\nu)\mu^n} \frac{\zeta^{n-1}}{\left(1+\frac{2n}{(1+|\rho|)\mu}\zeta,\right)^{n+\nu}} \tag{23}$$

where k is determined by the fact that

$$\int_0^\infty f_Z(\zeta) d\zeta = 1$$

to

$$k = \frac{\Gamma(n)\Gamma(\nu)\mu^n\gamma^n}{n^n B(n,\nu)}, \tag{24}$$

where $B(a,b) = \Gamma(a)\Gamma(b)/\Gamma(a+b)$ is the Beta-function. Inserting (24) into (23) finally results in

$$f_Z(\zeta) = \frac{\gamma^n}{B(n,\nu)} \frac{\zeta^{n-1}}{(1+\gamma\zeta)^{n+\nu}} \tag{25}$$

where

$$\gamma = \frac{2n}{\mu(1+|\rho|)}.$$

The density (25) looks similar to a F-distribution and belongs to the class of so-called $\mathcal{G}_I^0$-distribution which was originally introduced as the statistic for SAR image intensities [3]. For convenience it will hereafter be called the polynominal or p-distribution.

The r-th moment $E\zeta^r$ can be calculated by

$$\begin{aligned} m_r := E\zeta^r &= \int_0^\infty \zeta^r f_Z(\zeta) d\zeta \\ &= \frac{\gamma^n}{B(n,\nu)} \int_0^\infty \frac{\zeta^{n+r-1}}{(1+\gamma\zeta)^{n+\nu}} d\zeta \\ &= \gamma^{-r} \frac{B(n+r,\nu-r)}{B(n,\nu)} = \gamma^{-r} \frac{\Gamma(n+r)\Gamma(\nu-r)}{\Gamma(n)\Gamma(\nu)} \end{aligned} \tag{26}$$

By using the first moment m_1, γ can be expressed as

$$\gamma = \frac{B(n+1,\nu-1)}{B(n,\nu)} \frac{1}{m_1}. \tag{27}$$

Condsidering that the interferogram's magnitude might be normalized with respect to its expectation, i.e. $m_1 = 1$, the density function in (25) is often characterized by only a single shape parameter ν. Figs. 17 and 18 are exemplary illustrations of the density of the p-distribution for different number of looks and different shape parameters. It is important to note that the p-distribution tends towards the conventional distribution for the Gaussian backscatter model in (9) as the parameter ν increases. Thus, the conventional Gaussian density is included as a special case. The degree of heterogeneity can be measured with the estimated value of the parameter $\hat{\nu}$, i.e. if this value is estimated over two different areas, then the area with the larger value is more homogeneous.

In the Figs. 19 and 20 the accuracy of the new theoretical density is tested against the real measured data of Figs. 10 and 12 and compared to the Gaussian backscatter assumption. The determination of the shape or model parameter ν is described in section 4.1.3. It can be seen that the new multilook p-distribution fits, in both cases, the observed data much better than the corresponding density for the Gaussian assumption (dashed). The larger value of ν for patch 24 indicates higher homogeneity. An example with an even higher degree of heterogeneity is shown in the following section.

P516111.PDF [Page: 40 of 69]

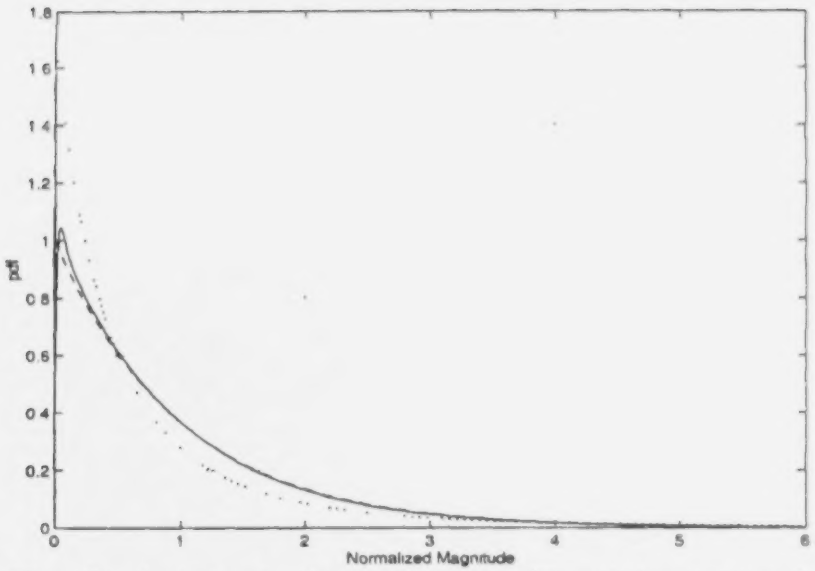

Figure 17 : *One-look density of p-distribution for different shape parameter.* $\nu = 2.5$ *(dotted),* $\nu = 50$ *(solid). Conventional interferogram magnitude for the Gaussian model (9) (dashed).*

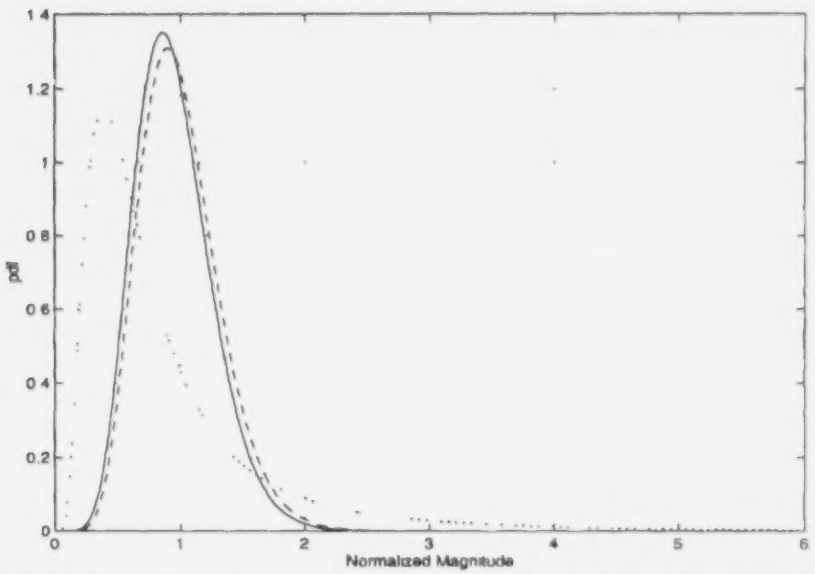

Figure 18 : *Ten-look density of p-distribution for different shape parameter.* $\nu = 2.5$ *(dotted),* $\nu = 50$ *(solid). Conventional interferogram magnitude for the Gaussian model (9) (dashed).*

P516111.PDF [Page: 41 of 69]

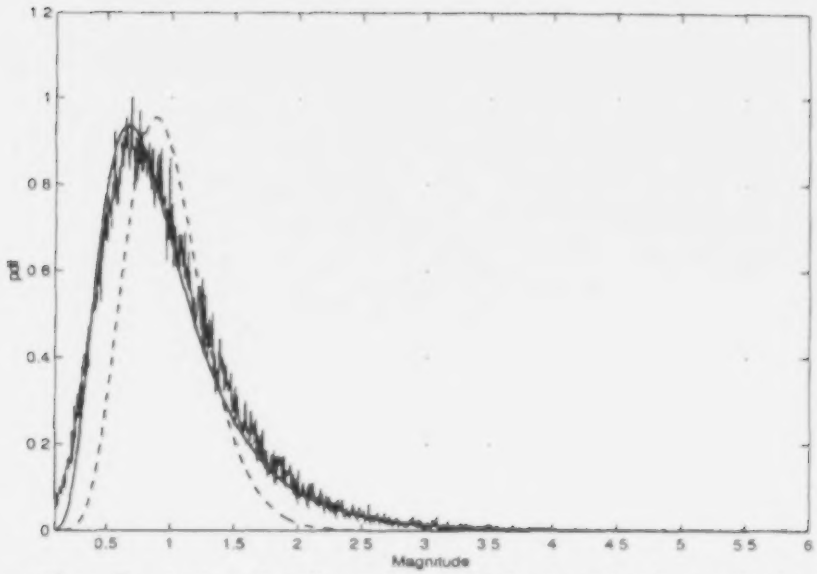

Figure 19 : *Ten-look p-density and empirical normalized magnitude density function of patch 1, $\nu = 7.6571$. Conventional interferogram magnitude for the Gaussian model (9) (dashed).*

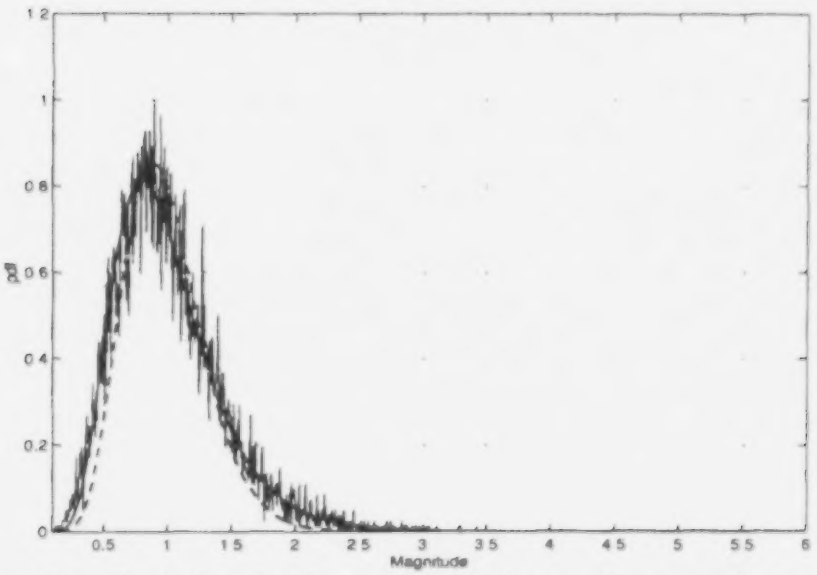

Figure 20 : *Ten-look p-density and empirical normalized magnitude density function of patch 24, $\nu = 17.1978$. Conventional interferogram magnitude for the Gaussian model (9) (dashed).*

4. CFAR Detector Scheme

This sections proposes a fully automatic detection scheme for slowly moving targets with constant false alarm rate (CFAR). All necessary parameters, such as effective number of looks, coherence and the model parameter ν are estimated directly from the dataset. The entire signal processing chain for the detection is schematically shown in the flow-chart of Fig. 21.

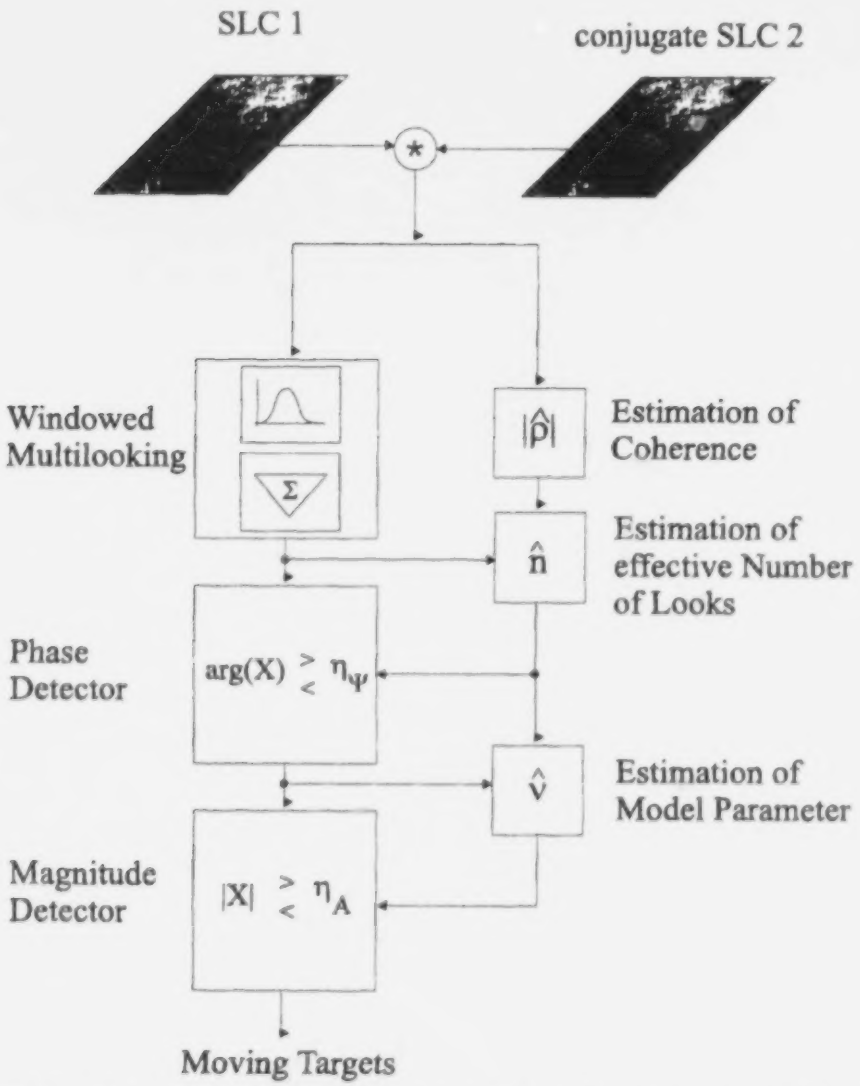

Figure 21 : *Flow-chart of the two-step ATI-MTI signal processing chain.*

4.1 Parameter Estimation

4.1.1 Coherence

Most commonly the magnitude of the correlation function (coherence) between the data of the two channels is estimated by replacing the expectation operator in (5) by the sample average

$$\hat{\rho} = \frac{\left|\sum_{k=1}^{K} z_1(k) z_2(k)^*\right|}{\sqrt{\sum_{k=1}^{K} |z_1(k)|^2 \sum_{k=1}^{K} |z_2(k)|^2}} \tag{28}$$

where K is the look number. In [11] it was analytically proved that the so-called sample coherence has the density

$$f_{\mathcal{R}}(\hat{\rho}) = 2(K-1)\left(1-\rho^2\right)^K \hat{\rho}\left(1-\hat{\rho}^2\right)^{K-2} {}_2F_1(K,K,1,(\rho\hat{\rho})^2). \tag{29}$$

Using (29) it can be shown that the estimation $\hat{\rho}$ is biased, particularly for small coherence values $\rho < 0.5$. This bias decreases with increasing number of independent looks K. In [19] a Maximum-Likelihood (ML) estimator of the coherence was derived based on the multivariate density function of the two channel complex data. It has been shown that this ML estimate is always smaller than or equal to the sample coherence. Since the correlation for along-track interferometry is high ($|\rho| > 0.8$), sample coherence bias is negligible in all practical cases.

4.1.2 Effective Number of Looks

The other parameter, besides the coherence, which characterizes the distributions of phase and magnitude, is the number of independent samples taken to average the interferogram. This parameter is traditionally called number of looks, based on a special SAR-image processing technique to reduce the "speckle noise", e.g. [20, 21]. All multilook pdfs were derived under the assumption that the pixels in the interferogram are independent. After matched filtering in the SAR processor the samples are usually no longer independent, and the effective number of looks is smaller than the number of samples averaged. Analytic consideration of the correlation between samples in the derived pdfs is very difficult and may be not possible at all. When the effective, or sometimes called equivalent, number of looks is used instead of the nominal number, the statistics of the interferogram are well represented over the whole range of coherence [22]. In principle the value of n should be an integer. This is usually not the case because the mean over correlated samples is taken. All density functions are, however, valid for $n \in \mathbb{R}_+$.

To reduce sidelobes, at the expense of resolution, the complex interferogram is sometimes windowed before the multilook averaging. In the ATI-processor used in this report, for instance, overlapping Gauss weighting functions (Fig. 22) of form

$$f(x) = A \exp\left(-\frac{x^2}{2(L/2.354)^2}\right) \tag{30}$$

for $|x| < L$ and 0 elsewhere, have been applied [23] to the data.

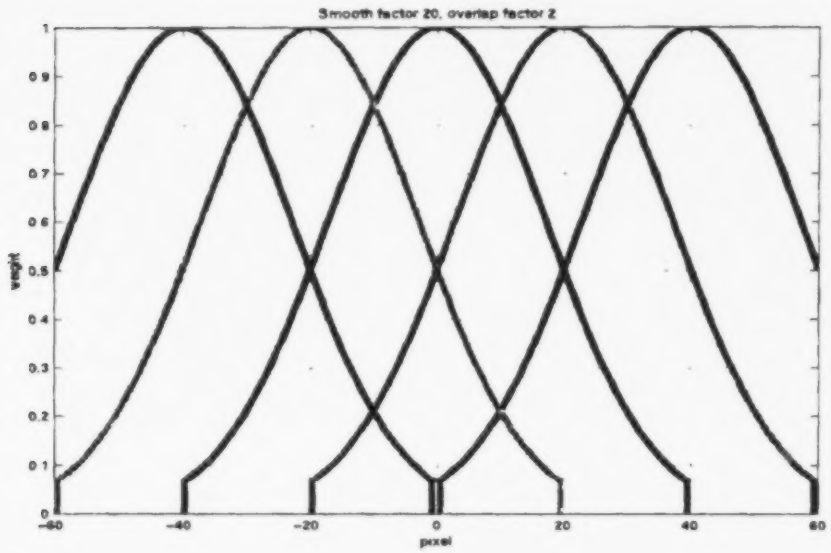

Figure 22 : *Window function of the interferometric processor.*

The length of the window $L = S \cdot O$ is controlled by the two independent parameters smooth, S, and overlap, O. The window repeats itself after S pixels and the width is adjusted by O. Let $\Delta x = v_0/B_{Dop}$ be the geometric SAR resolution , given as the ratio of platform velocity v_0 and the processed Doppler bandwidth B_{Dop}, and $\delta x = v_0/PRF$ be the pixel spacing. Then, the quotient $p = \Delta x/\delta x$ determines the number of correlated pixels in the SAR image assuming that the matched filter has been applied, e.g. [24]. As a rule of thumb, the number of looks is therefrom given as

$$\hat{n} = \frac{2L}{p} + 1 \tag{31}$$

where p is equal to $p = 4m/0.4m = 10$ for the Convair radar system used.

Since a more accurate estimation for the number of looks is required, a Maximum-Likelihood (ML) estimator of n is derived in the following. Maximum-Likelihood estimation is a technique for estimating constant parameters associated with random observations. This method takes the most likely parameter ϑ for a given set of observations $\underline{z}$ by maximizing the probability that the observations came from the distribution defined by the parameters. The parameter is determined by maximizing the Likelihood-function

$$L(\underline{z};\hat{\vartheta}) = \max_{\vartheta} f(\underline{z},\vartheta),$$

where $f(\cdot)$ denotes the density function of $\underline{Z}$, dependent on the parameter ϑ. By solving for the extrema of the density function (7) of the difference phase with respect to n, the most likely effective number of looks based on the observation is chosen. Assuming that the random vector $\underline{\Psi}$ [5] has mutually statistically independent elements $\Psi_1, \cdots, \Psi_K$, then its multivariate density function is given as the product of the single densities of (7)

$$f_{\underline{\Psi}}\left(\underline{\psi};n\right) = \prod_{k=1}^{K} f_{\Psi_k}\left(\Psi_k;n\right).$$

The ML estimator of n can be written as

$$f\left(\underline{\psi};\hat{n}\right) = \max_{n\in\mathbb{R}_+} f_{\underline{\Psi}}\left(\underline{\psi};n\right) = \max_{n\in\mathbb{R}_+} \prod_{k=1}^{K} f_{\Psi_k}\left(\psi_k;n\right).$$

or equivalently

$$L\left(\underline{\psi};\hat{n}\right) = \max_{n\in\mathbb{R}_+} \ln f_{\underline{\Psi}}\left(\underline{\psi};n\right) = \max_{n\in\mathbb{R}_+} \sum_{k=1}^{K} \ln f_{\Psi_k}\left(\psi_k;n\right). \qquad (32)$$

Accordingly, the function L is called the Log-Likelihood function. Fig. 23 shows for example the Log-Likelihood function for a nominal four-look interferogram ($S = 6, O = 2$) of patch 24, with a maximum at $\hat{n} = 4.49$. Since the number of correlated pixels in the SAR images is $p \cong 10$, only every 10-th pixel of the resulting interferogram has been taken to calculate the Likelihood function (in order to assure statistical independence between observations).

[5] Associated with the realizations of the phase differences $\psi_1, \cdots, \psi_K$.

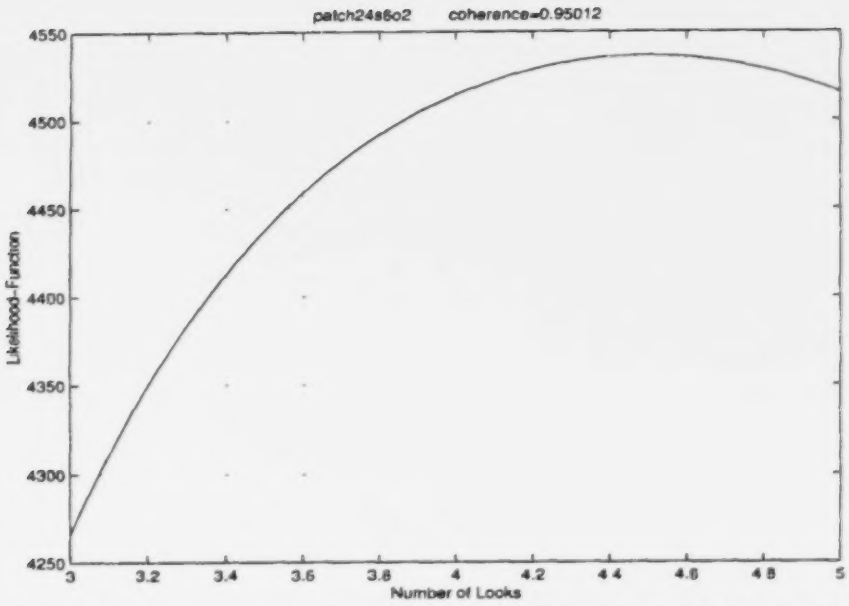

Figure 23 : *Log-Likelihood function versus number of looks for patch 24.*

Figs. 24 and 25 show the corresponding histograms superimposed to the theoretical density functions for both the rough estimation in (31) ($\hat{n} = 2*6*2/10+1 = 3.4$) and the ML estimate. There is much better agreement for the latter. A result based on simulated phase data in Fig. 26 shows that the proposed ML estimate for n is unbiased and normal distributed even for a relatively small number of samples $K = 10$.

Since the density function (7) is a highly nonlinear function its calculation and maximization is difficult and usually computationally time consuming. Using the gamma function derivative

$$\frac{d\Gamma(n)}{dn} = \Gamma(n)D(n)$$

and

$$\frac{d\ {}_2F_1(n,1,1/2,x)}{dn} = \sqrt{\pi}\sum_0^\infty \frac{\Gamma(n+k)}{\Gamma(n)\Gamma(k+1/2)}\left(D(n+k)-D(n)\right)x^{2k} \tag{33}$$

where $D(\cdot)$ is the so-called Psi or Digamma function [25], a numerically efficient iterative approach

$$\hat{n}_{m+1} = \hat{n}_m + \frac{L'\left(\underline{\psi}, \hat{n}_m\right)}{L''\left(\underline{\psi}, \hat{n}_m\right)}$$

based on Newton's algorithm can be used. L' and L'' are the first and second derivatives of the Log-Likelihood function with respect to n. In the case where n is an integer, the derivatives of (D.4) may be used rather than those given in (33).

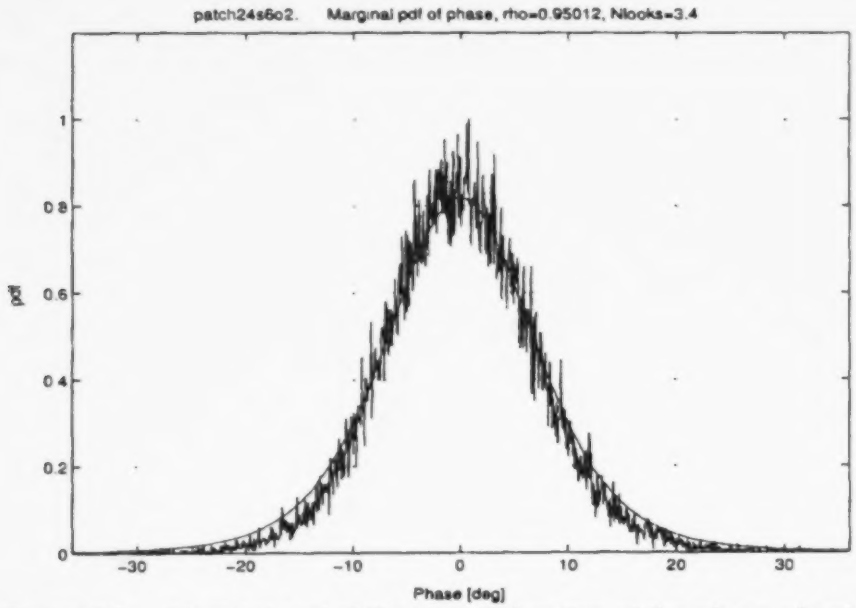

Figure 24 : *Marginal probability density function of the phase of patch 24 for an effective number of looks* $n = 3.4$.

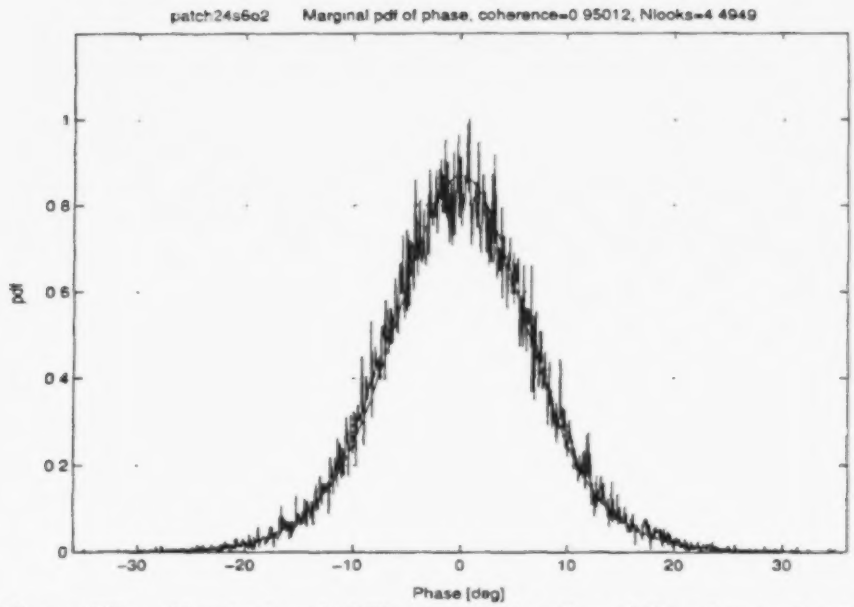

Figure 25 : *Marginal probability density function of the phase of patch 24 for an effective number of looks* $n = 4.49$.

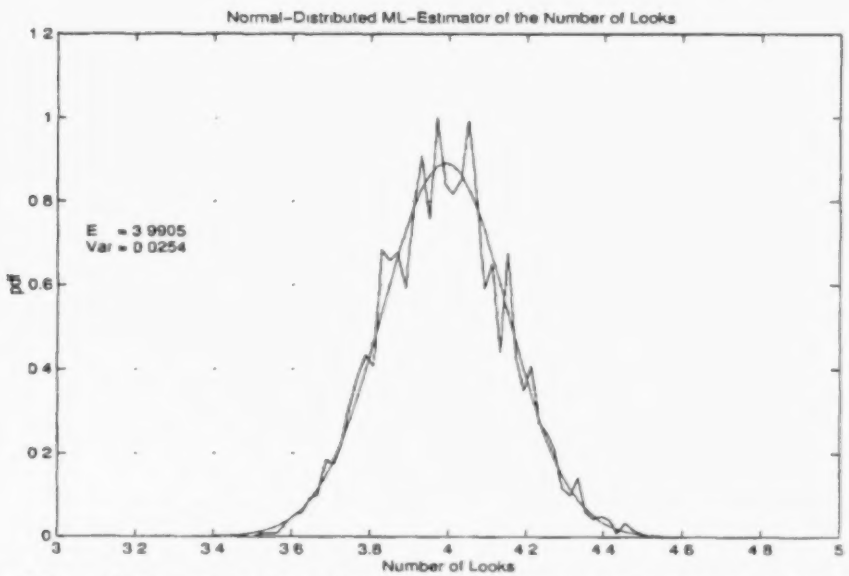

Figure 26 : *Histogram of the Maximum-Likelihood estimation of* n *for simulated phase data along with the normal distribution given by the plotted expectation and variance.*

4.1.3 Model Parameter ν

Using the moments in (26) it is possible to derive a closed form solution for the unknown model or shape parameter ν of the amplitude's density function in (25). This parameter indicates the degree of heterogenity of the underlying terrain. The first and second moment of the p-distribution are given as

$$\begin{aligned} m_1 &:= E\zeta = \frac{1}{\gamma}\frac{B(n+1,\nu-1)}{B(n,\nu)} \\ m_2 &:= E\zeta^2 = \frac{1}{\gamma^2}\frac{B(n+2,\nu-2)}{B(n,\nu)}. \end{aligned} \tag{34}$$

Forming the ratio m_1/m_2 leads to

$$\gamma = \frac{B(n+2,\nu-2)}{B(n+1,\nu-1)}\frac{m_1}{m_2}. \tag{35}$$

Inserting (35) into the first equation of (34) and using that $B(n,\nu) = \Gamma(n)\Gamma(\nu)/\Gamma(n+\nu)$ results in

$$\frac{\Gamma(n+1)^2\Gamma(\nu-1)^2}{\Gamma(n+2)\Gamma(\nu-2)\Gamma(n)\Gamma(\nu)} = \frac{m_1^2}{m_2}. \tag{36}$$

Using the identities for the Gamma-function given in [12]

$$\begin{aligned} \Gamma(\nu) &= (\nu-1)\Gamma(\nu-1) \\ &= (\nu-1)(\nu-2)\Gamma(\nu-2). \end{aligned} \tag{37}$$

which are valid for any real value of ν, yields

$$\frac{n(\nu-2)}{(n+1)(\nu-1)} = \frac{m_1^2}{m_2},$$

or equivalently as a solution for the unknown parameter,

$$\nu = \frac{2nm_2 - (n+1)m_1^2}{nm_2 - (n+1)m_1^2}. \tag{38}$$

Assuming that the interferogram amplitude is normalized to $m_1 = 1$, and having an estimate for the effective number of looks $\hat{n}$ (see subsection 4.1.2) as well as the computed estimation for the second moment

$$\hat{m_2} = \frac{1}{L}\sum_{l=1}^{L}\zeta_l^2,$$

(L denotes the number of used amplitude samples) an estimate $\hat{\nu}$ of the shape parameter can be computed by using (38). The effectiveness of this estimator has been previously demonstrated with the real data results shown in Figs. 19 and 20.

4.2 Test Statistics

Depending on the spatial scale of the resolution cell, the previously introduced density functions can be used to define a CFAR detector for slowly moving targets.

4.2.1 Small Resolution Cell Size

In the case where the dimension of the moving targets is on the order of the spatial geometric resolution of the SAR, a possible test statistic might be the comparison of the cell's phase and amplitude with suitably chosen thresholds. This assumption means that the backscatter power contained in the cell mainly results from the desired target and that the clutter (or speckle) power is negligible. The threshold can be determined as the α-percentile of the pdf in (7), where α denotes a given false alarm rate. Integration of the highly nonlinear density function (7) with respect to the phase to determine the threshold is analytically very difficult or may even be impossible. Hence, numerical integration has to be used. Fig. 27 shows the relation between the desired threshold η_ψ and the given false alarm probability α. This probability can be recognized as the corresponding region under the phase density function.

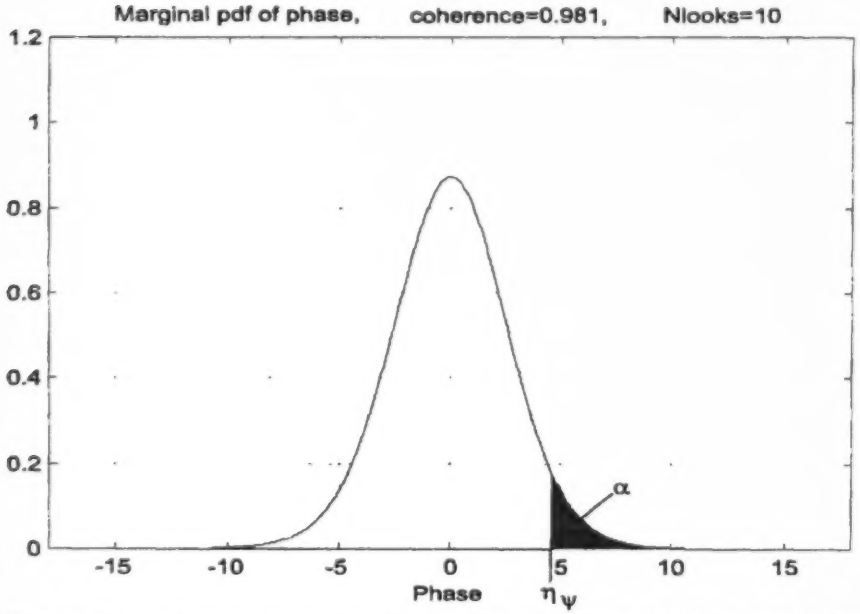

Figure 27 : Phase threshold for the moving target detector depending on the given false alarm probability.

The false alarm rate for the phase detector can be further reduced by taking into account the fact that stationary targets (clutter pixels) with large phase values most likely have a small amplitude. This statistical behaviour can, for instance, be recognized from the joint distribution of the phase and amplitude in Figs. 3 and 4. Therefore, a second step in the test for the remaining pixels can be the comparison of their amplitudes with a threshold η_Z. Assuming the estimate of the model or shape parameter ν has been computed via (38), this amplitude threshold can be determined in closed form from the pdf in (25). The corresponding multilook probability function of the amplitudes density or p-distribution is given as

$$F_Z(\zeta) = \int_0^\zeta f_Z(a)da = \frac{\gamma^n}{B(n,\nu)} \int_0^\zeta \frac{a^{n-1}}{(1+\gamma a)^{n+\nu}} da$$
$$= \frac{\gamma^n}{B(n,\nu)} \frac{\zeta^n}{n} \, {}_2F_1\,(n+\nu, n; 1+n, -\gamma\zeta) \qquad (39)$$

with $\gamma = B(n+1,\nu-1)/B(n,\nu)$. It can be seen from (39) that the probability function, and therefore the threshold, is independent of the coherence $|\rho|$ due to normalization. In Fig. 28 the probability function of the p-distribution is plotted along with the amplitude threshold η_Z for a given false alarm rate α.

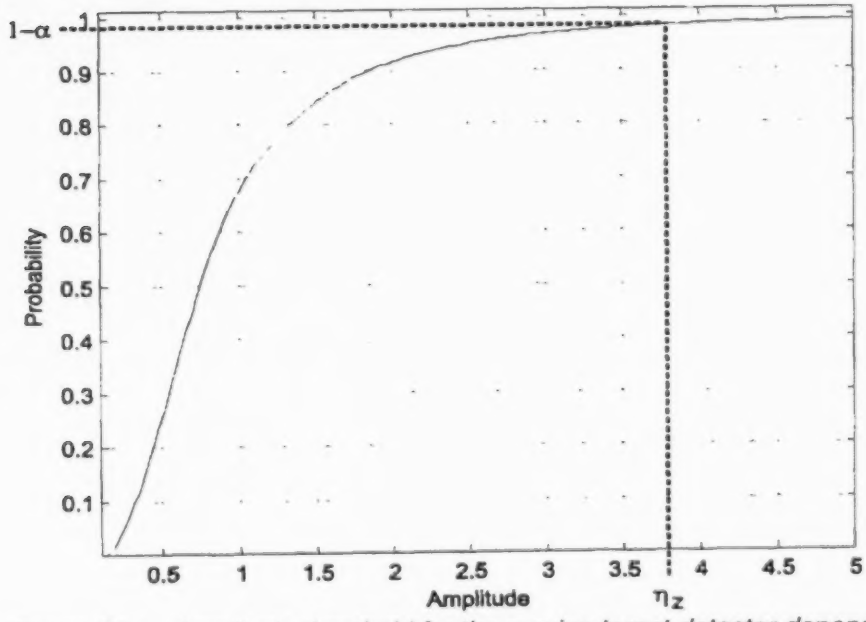

Figure 28 : *Amplitude threshold for the moving target detector depending on the given false alarm probability.*

4.2.2 Large Resolution Cell Size

In cases where the spatial resolution is much larger than the target size, the clutter power can no longer be neglected. Here, the hypothesis"clutter only" has to be tested against the alternative"clutter plus target". Hence, the test problem might be characterized as:

$$\begin{array}{ll} \underline{X} = a + \underline{\Psi}. & \Psi_i \quad \text{have pdf (7)} \\ & a \in \mathbb{R} \\ \text{Hypothesis} & H : a = 0 \\ \text{Alternative} & K : a \neq 0. \end{array} \tag{40}$$

(41)

The test statistic can be derived, for instance, via a Maximum-Likelihood-quotient criterion, see e.g. [26, 27]. This criterion requires the maximal value of the ratio

$$t(\underline{x}) = \frac{\sup_{a \in \mathbb{R}/\{0\}} f_{\underline{X}}(\underline{x}; a)}{f_{\underline{X}}(\underline{x}; 0)} = \frac{f_{\underline{X}}(\underline{x}; \hat{a})}{f_{\underline{X}}(\underline{x}; 0)} \tag{42}$$

where $\hat{a}$ denotes the Maximum-Likelihood estimator of a and the density function $f_{\underline{X}}(\underline{x})$ is given by (7). The test $t(\underline{x})$ has to be compared to a threshold:

$$T(\underline{x}) = \begin{cases} 1 & , \quad \text{if} \quad t(\underline{x}) > \eta \\ 0 & , \quad \text{else} \end{cases}$$

The threshold η has to be determined for a given false alarm probability α. To derive such a threshold is generally very complicated and an open issue for the moving target detector. In some cases the asymptotic result given in [28] can be used. It states, that, $2 \ln t(\underline{X})$ is χ^2_1-distributed (under the hypothesis) asymptotically for large k, where k denotes the number of samples. Therefore, the threshold can be chosen as

$$\eta = \exp\left(\frac{1}{2}\chi^2_{1,\alpha}\right)$$

assuming that k is large. Herein, $\chi^2_{1,\alpha}$ means that number which is exceeded by a chi-square distributed random variable with probability α. One way to verify the suitability of such a test and threshold could be to have the SAR raw data re-processed with a lower geometric resolution.

4.3 Results

The aim of this section is to demonstrate the capability of the proposed detector to detect slowly moving targets based on real measured SAR data. The imagery used, was collected during the Petawawa experiment 1999. The test site was comprised of composite terrain containing a part of a highway, forests and areas with shrubby vegetation. It also included a marked-off area with numerous objects used as artillery targets including different military vehicles, see Fig. 31. The entire processing chain depicted in Fig. 21 has been executed. The coherence was estimated to $\hat{\rho} = 0.97187$ and the effective number of looks via MLE to $\hat{n} = 12.86$. The theoretical phase density function for these parameters is plotted in Fig. 29, and is superimposed over the histogram. The almost perfect agreement of the two curves can be clearly recognized. It confirms the validity of the multiplicative clutter model even for extended heterogeneous surfaces consisting of composite terrain.

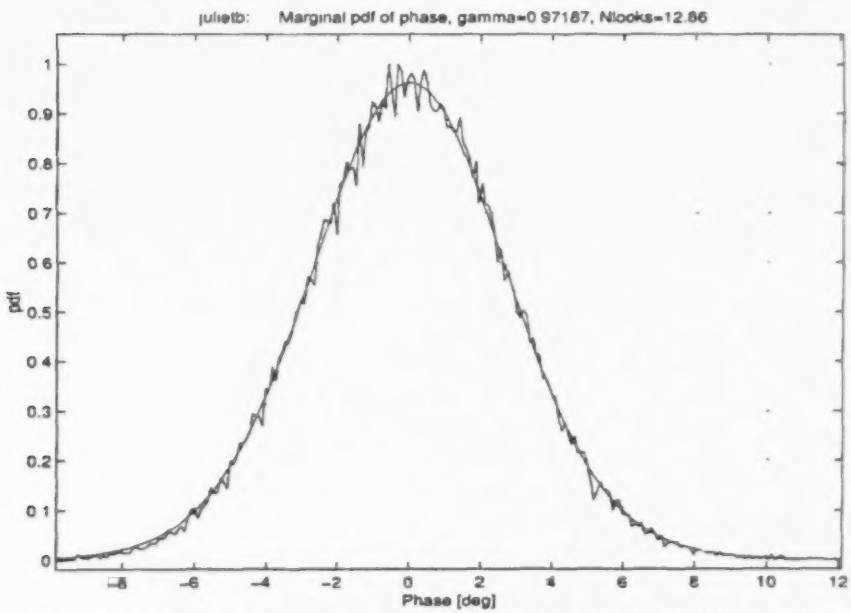

Figure 29 : *Histogram of the interferometric phase for the highway area along with the theoretical probability density function.*

Inherent phase errors probably caused by mismatched SAR processing or signal reflections on mechanical antenna/platform structures have been eliminated prior to the detection. In fact, the phase values have been calibrated to zero mean by removing any linear trend included in the phase data. The trend was estimated in a least mean square sense.

The corresponding histogram of the scene's magnitude is shown in Fig. 30 along with the p-distribution for an estimated model parameter $\hat{\nu} = 6.9739$. The relatively small value of ν indicates a large degree of heterogeneity in the underlying terrain. To demonstrate the improved agreement of the new p-distribution with the real data, the original magnitude density derived under the homogeneous backscatter assumption is also plotted.

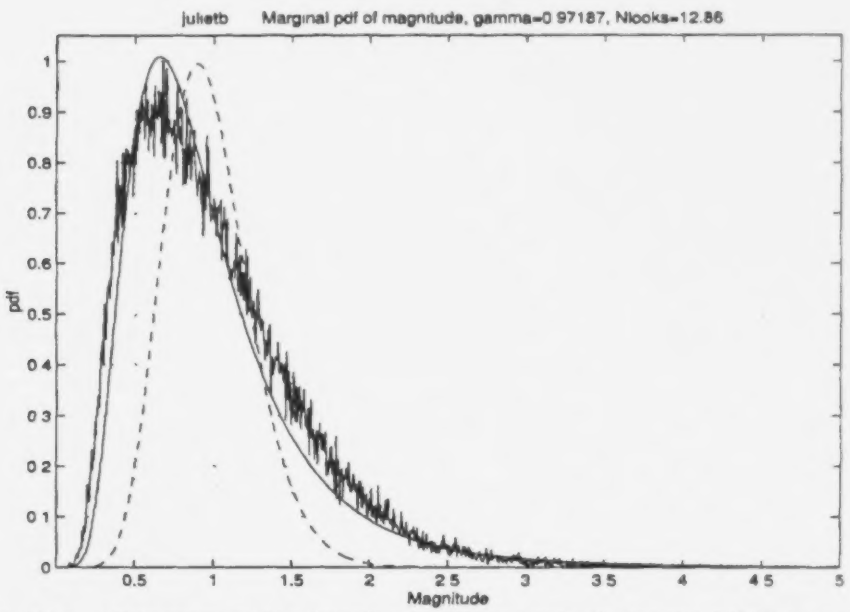

Figure 30 : *Histogram of the interferometric magnitude for the highway area along with the p-distribution (solid) and the original magnitude pdf (dashed).*

Even though the p-distribution shows a slight deviation from the real data for smaller amplitudes, the larger magnitudes match accurately. For MTI this property is the crucial one since the shape of the tail determines the detection thresholds. For the afore mentioned values of $\hat{\rho}, \hat{n}$ and $\hat{\nu}$, CFAR thresholds were computed for two different false alarm rates $\alpha = 2.5 \cdot 10^{-5}$ and $\alpha = 1.0 \cdot 10^{-6}$. While the false alarm rate for the phase was held fixed at $\alpha = 0.005$, the value for the magnitude was chosen to be either $\alpha = 0.005$ or $\alpha = 0.0002$. The calculated threshold for the phase was $\eta_\psi = 7.3874$ degrees and for the magnitudes $\eta_\zeta = 4.9049$ and $\eta_\zeta = 11.9720$, respectively. Fig. 31 shows the resulting detections. For the higher false alarm rate, five targets are detected, four of them known to be stationary from ground-truth data (marked by squares), i.e. those are actual false alarms. After lowering the false alarm rate only the correct moving target remained (marked by a circle). As mentioned before, the proposed

detector scheme works only for slowly (compared to the platform) moving targets which are still well focused by the stationary reference function. This can be recognized in this example because it is known that there were several fast moving vehicles on the highway during the measurement as well. Those targets are highly defocused and smeared, i.e. their energy is spread over an extended area, they are blurred and have disappears in the clutter.

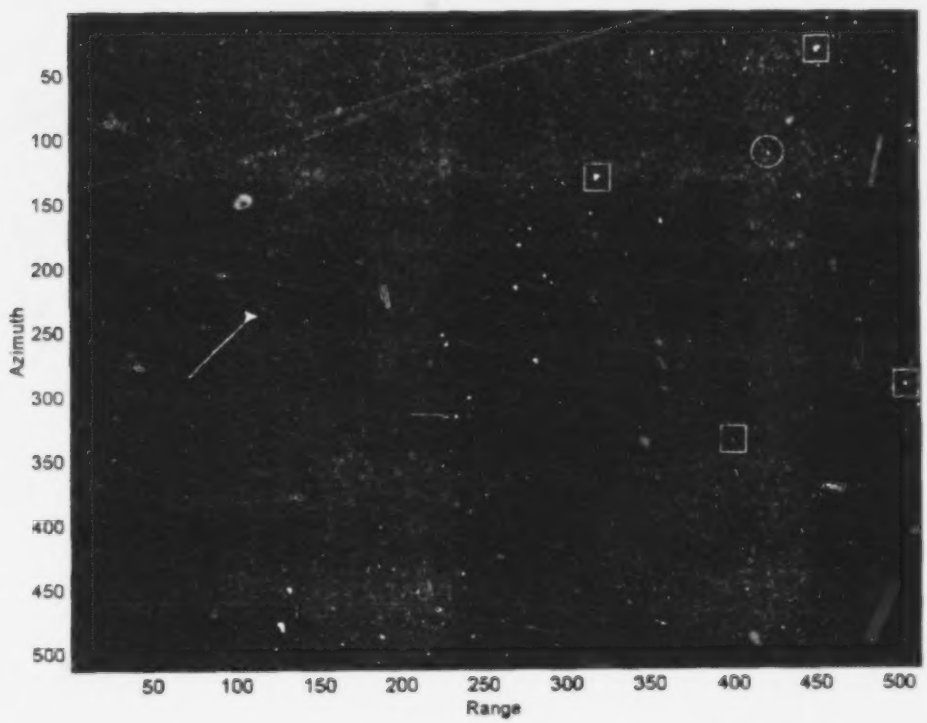

Figure 31 : *SAR image of the Petawawa target area used for slow moving target detection. All marked detections correspond to* $\alpha = 2.5 \cdot 10^{-5}$*, whereas the circled target relates to* $\alpha = 1 \cdot 10^{-6}$*. The arrow indicates an undetected fast mover.*

P516111.PDF [Page: 56 of 69]

5. Conclusions

In this report, a fully automatic detection scheme for slow moving targets within SAR ATI imagery has been developed, which exploits the phase differences of the radar returns from two independent receivers. This so called along-track interferometric detector is based on an accurate statistical characterization of the phase and magnitude of the interferogram.

It was shown with real airborne SAR data that the conventional density function of the phase, derived under the assumption of homogeneous clutter with Gaussian backscatter, agrees almost perfectly with reality even for highly heterogeneous clutter. It was demonstrated that this is due to an underlying multiplicative model of the backscatter distribution, where the multiplicative random variable cancels out when the phase is computed. In contrast, this term remains in the magnitude and causes, therefore, strong deviation between the theoretical and measured data.

Motivated by this discrepancy, a novel distribution was derived for the interferogram's magnitude. This pdf, called p-distribution was shown to match the real data much more accurately, particularly for extremely heterogeneous composite terrain. Estimation procedures for all involved parameters were derived and their suitability proven with real data. Since many of the introduced density functions contain indefinite power series which tend to infinity, the problem of numerical stability in practical implementations was also addressed. In fact, recursive algorithms have been proposed based on asymptotic expansions of Gauss' hypergeometric function.

Since the emphasis of this study was on the detection of slow ground moving targets, future work will have to focus on different open items. Fast moving objects (compared to the platform velocity) are highly defocused by the SAR processor which causes them to blur or even fully disappear in the SAR image. Since the proposed detector does not work for such targets, different methods have to be developed, for instance, based on Doppler filtering etc. However, for spaceborne SAR systems this effect can be neglected for ground moving vehicles. Even if targets are well focused, the problem of a large displacement of the movers arises, i.e. the image of the moving target appears in the wrong location on the stationary SAR image. Therefore, the accurate estimation of the correct position and speeds are also open issues.

P516111.PDF [Page: 57 of 69]

References

1. Yueh, S. H. and Kong, J. A. (1989). K-Distribution and Polarimetric Terrain Clutter. *J. of Electromagnetic Waves and Applications*, **3**(8), 747–768.

2. Joughin, I. R., Winebrenner, D. P. and Percival, D. B. (1994). Probability Density Functions for Multilook Polarimetric Signatures. *IEEE Trans. Geoscience and Remote Sensing*, **GRS-32**(3), 562–574.

3. Frery, A. C., Müller, H.-J., Yanasse, C. F. and Sant'Anna, S. J. S. (1997). A Model for Extremely Heterogeneous Clutter. *IEEE Trans. Geoscience and Remote Sensing*, **GRS-35**(3), 648–659.

4. Livingstone, C., Sikaneta, I., Gierull, C.H., Chiu, S., Beaudoin, A., Campbell, J., Beaudoin, J., Gong, S. and Knight, T. (2001). An Airborne SAR Experiment to Support RADARSAT-2 GMTI. *subm. to Canadian Journal of Remote Sensing*.

5. Goodman, J. W. (1976). Some Fundamental Properties of Speckle. *J. Opt. Soc. Am.*, **66**(11), 1145–1150.

6. Goodman, J. W. (1963). Statistical Analysis Based on a Certain Multivariate Complex Gaussian Distribution (An Introduction). *Ann. Math. Stat.*, **34**(152), 152–180.

7. Lee, J.-S., Hoppel, K. W., Mango, S. A. and Miller, A. R. (1994). Intensity and Phase Statistics of Multilook Polarimetric and Interferometric SAR Imagery. *IEEE Trans. Geoscience and Remote Sensing*, **GRS-32**(5), 1017–1028.

8. Lee, J.-S., Miller, A. R. and Hoppel, K. W. (1994). Statistics of Phase Difference and Product Magnitude of Multi-Look Processed Gaussian Signals. *Waves in Random Media*, **4**, 307–319.

9. Touzi, R. and Lopes, A. (1996). Statistics of the Stokes Parameters and of the Complex Coherence Parameters in One-Look and Multilook Speckle Fields. *IEEE Trans. Geoscience and Remote Sensing*, **GRS-34**(2), 519–531.

10. Hagberg, J. O., Ulander, L. M. H. and Askne, J. (1995). Repeat-Pass SAR Interferometry Over Forested Terrain. *IEEE Trans. Geoscience and Remote Sensing*, **GRS-33**(3), 331–340.

11. Touzi, R., Lopes, A. , Bruniquel, J. and Vachon, W. (1999). Coherence Estimation for SAR Imagery. *IEEE Trans. Geoscience and Remote Sensing*, **GRS-37**(1), 135–149.

P516111.PDF [Page: 58 of 69]

12. Abramowitz, M. and Stegun, I. A. (1970). Handbook of Mathematical Functions, 9 ed. Dover Publications, Inc.

13. Just, D. and Bamler, R. (1994). Phase Statistics of Interferograms with Applications to Synthetic Aperture Radar. *Applied Optics*, **33**(20), 4361–4367.

14. Papoulis, A. (1991). Probability, Random Variables and Stochastic Processes, 3 ed. McGraw Hill Inc.

15. Livingstone, C. (2000). Multiplicative Phase Noise. Personal Communication.

16. Conte, E., Longo, M. and Lops, M. (1991). Modelling and Simulation of Non-Rayleigh Radar Clutter. *IEE Proc.-Radar, Sonar Navig. (Pt. F)*, **138**(2), 121–130.

17. Tur, M., Chin, K. C. and Goodman, J. W. (1982). When is Speckle Noise Multiplicative?. *Applied Optics*, **21**(20), 1157–1159.

18. Jakeman, E. and Tough, R. J. A. (1987). Generalized K Distribution: A Statistical Model for Weak Scattering. *J. Opt. Soc. Am.*, **4**(9), 1764–1772.

19. Seymour, M. S. and Cumming, I.G. (1994). Maximum Likelihood Estimation For SAR Interferometry. In *Proc. of IGARSS'94*, pp. 2272–2275. Pasadena, CA.

20. Franceschetti, G. and Lanari, R. (1999). Synthetic Aperture Radar Processing, CRC Press.

21. Soumekh, M. (1999). Synthetic Aperture Radar Signal Processing with MATLAB Algorithms, John Wiley & Sons Inc.

22. Joughin, I. R. and Winebrenner, D. P. (1994). Effective Number of Looks for a Multilook Interfeometric Phase Distribution. In *Proc. of IGARSS'94*, pp. 2276–2278. Pasadena, CA.

23. Sikaneta, I. (2000). Smoothing and Overlap in the ATInSAR Processor. Technical (Lab) Note, Radarsat2 Project, Defence Research Establishment Ottawa.

24. Gierull, C. H. (2000). Statistical Properties of the Noise behind the SAR-processor. Technical (Lab) Note, Radarsat2 Project, Defence Research Establishment Ottawa.

25. Gradshteyn, I. S. and Ryzhik, I. M. (2000). Table of Integrals, Series and Products (Sixth Edition), 6 ed. Academic Press.

P516111.PDF [Page: 59 of 69]

26. Böhme, J. F. (1993). Stochastische Signale, Stuttgart: Teubner-Verlag.

27. Novak, L. M., Sechtin, M. B. and Cardullo, M. J. (1989). Studies on Target Detection Algorithms That Use Polarimetric Radar Data. *IEEE Trans. Aerosp. and Electron. Systems*, **AES-25**(2), 150–165.

28. Wittig, H. and Nölle, G. (1970). Angewandte Mathematische Statistik, Stuttgart: Teubner-Verlag.

Annex A
Limit of the Conditional Variance of the Phase

Using (14), the conditional density function of the phase for a fixed (but large) magnitude is given as

$$f_{\Psi|\mathcal{E}=\eta}(\psi|\eta) \cong \frac{\sqrt{2\pi\alpha}}{2\pi}\exp\left(\alpha(\cos\psi - 1)\right)/g(\alpha) \tag{A.1}$$

where

$$\alpha = \frac{2n|\rho|\eta}{(1-|\rho|^2)} \qquad \text{and} \qquad g(\alpha) = \left(\sum_{k=0}^{K}(-1)^k \frac{\Gamma\left(k+\frac{1}{2}\right)}{\Gamma(k+1)\Gamma\left(\frac{1}{2}-k\right)}\frac{1}{(2\alpha)^k}\right).$$

Since α is assumed to be large, the fluctuation of the phase around zero will be relatively small, so that the Taylor-series expansion

$$\cos\psi \cong 1 - \frac{\psi^2}{2} \tag{A.2}$$

at $\psi_0 = 0$ can be used [6]. Inserting (A.2) into (A.1) yields

$$f_{\Psi|\mathcal{E}=\eta}(\psi|\eta) \cong \frac{\sqrt{2\pi\alpha}}{2\pi}\exp\left(-\frac{\alpha\psi^2}{2}\right)/g(\alpha). \tag{A.3}$$

As the the conditional expectation is zero, the conditional variance can then be calculated as the integral

$$\begin{aligned}
\mathrm{var}(\Psi|\mathcal{E}=\eta) &\cong \int_{-\infty}^{\infty}\psi^2 f_{\Psi|\mathcal{E}=\eta}(\psi|\eta)d\psi \\
&= 2\frac{\sqrt{2\pi\alpha}}{2\pi}/g(\alpha)\int_0^{\infty}\psi^2\exp\left(-\frac{\alpha\psi^2}{2}\right)d\psi \\
&= 2\frac{\sqrt{2\pi\alpha}}{2\pi}/g(\alpha)\frac{\sqrt{\pi}}{4(\alpha/2)^{3/2}} \\
&= \frac{1}{\alpha g(\alpha)} = O\left(\frac{1}{\alpha}\right) \overset{\eta\to\infty}{\longrightarrow} 0
\end{aligned} \tag{A.4}$$

for all $0 < |\rho| < 1$.

[6] The error $\varepsilon = \cos\psi - 1 + \psi^2/2$ is for example smaller than $\varepsilon = 5\cdot 10^{-5}$ when $|\psi| < 12$ degrees.

Annex B
The Noncentral Inverse Chi-Square Distribution

Let the random variables Z_n be mutually independent complex standard normal distributed $Z \sim \mathcal{N}^{\mathbb{C}}(0,1)$ [7] with density

$$f_Z(z) = \frac{1}{2\pi}\exp\left(-z^H z\right),$$

then the random variable $X = \sum_{n=1}^{\nu} Z_n^2$ is Chi-square distributed with 2ν-degrees of freedom $X \sim \chi^2_{2\nu}$ and density [12]

$$f_X(x) = \frac{1}{2^\nu \Gamma(\nu)} x^{\nu-1}\exp(-x/2) \qquad x > 0. \tag{B.1}$$

Further, let $\mu > 0$ and $\gamma \geq 0 \in \mathbb{R} > 0$, so that $Y = \mu/(X+\gamma)$, then the random variable Y is said to be noncentral inverse Chi-square distributed $Y \sim \chi^{-2}_{2\nu}(\mu,\gamma)$ with 2ν-degrees of freedom, shape parameter μ, noncentrality parameter γ and density

$$f_Y(y) = \frac{\mu(\mu-\gamma y)^{\nu-1}}{2^\nu\Gamma(\nu)}\left(\frac{1}{y}\right)^{\nu+1}\exp\left(-\frac{\mu-\gamma y}{2y}\right) \qquad 0 < y < \frac{\mu}{\gamma}. \tag{B.2}$$

Proof:
The cumulative probability function of Y is given as

$$\begin{aligned} F_Y(y) &= \mathrm{P}\{Y \leq y\} = \mathrm{P}\left\{\frac{\mu}{X+\gamma} \leq y\right\} = \mathrm{P}\left\{X \geq \frac{\mu-\gamma y}{y}\right\} \\ &= 1 - \mathrm{P}\left\{X \leq \frac{\mu-\gamma y}{y}\right\} = 1 - F_X\left(\frac{\mu-\gamma y}{y}\right). \end{aligned} \tag{B.3}$$

The density function can be calculated as the derivative of (B.3)

$$\begin{aligned} f_Y(y) &= \frac{dF_Y(y)}{dy} = -f_X\left(\frac{\mu-\gamma y}{y}\right)\left(-\frac{\mu}{y^2}\right) \\ &= \frac{1}{2^\nu\Gamma(\nu)}\left(\frac{\mu-\gamma y}{y}\right)^{\nu-1}\frac{\mu}{y^2}\exp\left(-\frac{\mu-\gamma y}{2y}\right) \qquad 0 < y < \frac{\mu}{\gamma}. \end{aligned} \tag{B.4}$$

[7] The real- and imaginary part of Z are statistically independent standard normal distributed $\sim \mathcal{N}^{\mathbb{R}}(0,1/2)$.

For the interesting special case of $\gamma = 0$, i.e. the central inverse Chi-square distribution, the density function in (B.4) is

$$f_Y(y) = \frac{\mu^\nu}{2^\nu \Gamma(\nu)} \left(\frac{1}{y}\right)^{\nu+1} \exp\left(-\frac{\mu}{2y}\right)$$
$$= \frac{\tilde{\mu}^\nu}{\Gamma(\nu)} \left(\frac{1}{y}\right)^{\nu+1} \exp\left(-\frac{\tilde{\mu}}{y}\right) \qquad \tilde{\mu}, \nu, y > 0 \qquad \text{(B.5)}$$

Annex C
Probability Density Function of the Multilook Sample Covariance Matrix for Non-Gaussian Clutter

Let the sample covariance matrix $\hat{\mathbf{R}} = \sum_{k=1}^{n} \underline{X}\underline{X}^H \in \mathbb{C}^{m\times m}$ be complex Wishart distributed $\hat{\mathbf{R}} \sim \mathcal{W}^{\mathbb{C}}(n, \mathbf{R})$ [6]. Further, let the real random variable X be central inverse Chi-square distributed with 2ν degrees of freedom and shape parameter μ, $X \sim \chi^{-2}_{2\nu}(\mu)$ and the density given by (B.5). The product matrix $\mathbf{Q} = X\hat{\mathbf{R}}$ has the probability density function

$$f_{\mathbf{Q}}(\mathbf{q}) = \frac{\mu^{\nu}\det(\mathbf{q})^{n-m}}{I_m(\mathbf{R})\Gamma(\nu)}\left(\frac{1}{\mu+\operatorname{tr}\{\mathbf{R}^{-1}\mathbf{q}\}}\right)^{n+\nu-m+1}. \tag{C.1}$$

with $I_m(\mathbf{R}) = \pi^{m(m-1)/2}\Gamma(n)\cdots\Gamma(n-m+1)\det(\mathbf{R})^n$.

Proof:

The density function of a product $Z = XY$ of two random variables can be calculated via

$$f_Z(z) = \int_{-\infty}^{\infty} \frac{1}{|w|} f_{XY}\left(\frac{z}{w}, w\right) dw, \tag{C.2}$$

where $f_{XY}(x,y)$ denotes the joint density function [14]. In the case where X and Y are independent, the joint density can be replaced by the product of the single densities. Using (C.2) and (3), the density of $\mathbf{Q}$ can be expressed as

$$\begin{aligned} f_{\mathbf{Q}}(\mathbf{q}) &= \int_0^{\infty} \frac{1}{w} f_X(w) f_{\hat{\mathbf{R}}}\left(\frac{\mathbf{Q}}{w}\right) dw \\ &= \frac{\mu^{\nu}\det(\mathbf{q})^{n-m}}{I_m(\mathbf{R})\Gamma(\nu)} \int_0^{\infty} \left(\frac{1}{w}\right)^{n+\nu-m+2} e^{-\frac{1}{w}\left(\mu+\operatorname{tr}\{\mathbf{R}^{-1}\mathbf{Q}\}\right)} dw \end{aligned} \tag{C.3}$$

Substituting $t = 1/w$ in (C.3) leads to

$$f_{\mathbf{Q}}(\mathbf{q}) = \frac{\mu^{\nu}\det(\mathbf{q})^{n-m}}{I_m(\mathbf{R})\Gamma(\nu)} \int_0^{\infty} t^{n+\nu-m} \exp\left(-\left(\mu+\operatorname{tr}\{\mathbf{R}^{-1}\mathbf{Q}\}\right)t\right) dt.$$

Using the integral identity in [25] yields (C.1).

Annex D
Practical Implementations of the PDF's

D.1 Asymptotic Expansion of Modified Bessel Functions

For large arguments x, the modified Bessel function I of order ν can asymptotically be written as [25, 12]

$$I_\nu(x) \cong \frac{\exp(x)}{\sqrt{2\pi x}} \left(\sum_{k=0}^{K} (-1)^k \frac{\Gamma\left(\nu+k+\frac{1}{2}\right)}{\Gamma(k+1)\Gamma\left(\nu+\frac{1}{2}-k\right)} \frac{1}{(2x)^k} \right), \tag{D.1}$$

and the modified Bessel function K of order ν as

$$K_\nu(x) \cong \frac{\sqrt{\pi}\exp(-x)}{\sqrt{2x}} \left(\sum_{k=0}^{K} \frac{\Gamma\left(\nu+k-\frac{1}{2}\right)}{\Gamma(k+1)\Gamma\left(\nu+\frac{1}{2}-k\right)} \frac{1}{(2x)^k} \right). \tag{D.2}$$

where $\Gamma(\cdot)$ denotes the Gamma function. In order to avoid the use of the Gamma function, the sum-term on the right side of (D.1), can be re-written as

$$\sum_{k=0}^{K} (-1)^k \frac{\Gamma\left(\nu+k+\frac{1}{2}\right)}{\Gamma(k+1)\Gamma\left(\nu+\frac{1}{2}-k\right)} \frac{1}{(2x)^k} = \sum_{k=0}^{K} (-1)^k \frac{\prod_{l=1}^{k}[\mu-(2l-1)]}{k!\,(8x)^k},$$

where $\mu = 4\nu^2$. The upper limit K of summands is dependent upon the required accuracy.

D.2 Gauss' Hypergeometric Function for the Phase' PDF

Gauss' hypergeometric function ${}_2F_1(\cdot)$ is a special case of the generalized hypergeometric function ${}_nF_m(\cdot)$ and is defined as the infinite series [12],[25]

$$\begin{aligned} F(a,b;c;z) &= {}_2F_1(a,b;c;z) \\ &= \frac{\Gamma(c)}{\Gamma(a)\Gamma(b)} \sum_{k=0}^{\infty} \frac{\Gamma(a+k)\Gamma(b+k)}{\Gamma(c+k)} \frac{z^k}{k!}, \end{aligned} \tag{D.3}$$

where a, b, c are real scalars and z can be a complex value. Using Gauss' relation for the continuous function $F(a+1,b;c;z)$ [12],

$$F(a+1,b;c;z) = \frac{(2a-c-az+bz)}{a(1-z)} F(a,b;c;z) + \frac{(c-a)}{a(1-z)} F(a-1,b;c;z),$$

and assuming an integral number of looks n, a recursion formula for the hypergeometric function in the pdf (7) can be defined

$$F(n+1,1;1/2;z) = -\frac{2n-1/2-(n-1)z}{n(z-1)}F(n,1;1/2;z) + \frac{n-1/2}{n(z-1)}F(n-1,1;1/2;z). \tag{D.4}$$

The starting values for the iteration are given as

$$F(0,1;1/2;z) = 1 \tag{D.5}$$

and

$$F(1,1;1/2;z) = \sum_{k=0}^{\infty} \frac{1\cdot 2\cdot 3\ldots k}{1\cdot 3\cdot 5\ldots 2k-1}(2z)^k = \sum_{k=0}^{\infty} \frac{\Gamma(k+1)}{\Gamma(k+1/2)}z^k = \sum_{k=0}^{\infty} a_k z^k. \tag{D.6}$$

where $a_k = \Gamma(k+1)/\Gamma(k+1/2)$. Since the power series in (D.6) still has an infinite number of addends, convergence has to be ensured. The quotient criterion for the convergence of power series, for instance, demands that the limit of the ratio

$$\frac{a_{k+1}z^{k+1}}{a_k z^k} = \frac{k+1}{k+1/2}z \tag{D.7}$$

is smaller than one. From (D.7) it is necessary, that

$$\lim_{k\to\infty} \frac{a_{k+1}z^{k+1}}{a_k z^k} = z < 1.$$

This is, however, fulfilled for the density function of the phase in (7) because the argument $z = |\rho|^2\cos^2(\psi)$ is obviously always smaller than one, if $|\rho| < 1$.

If the effective number of looks, n, is a rational number, the value of $F(n,1,1/2,z)$ can be computed via an interpolation between the integral values. Here, it is more accurate when the natural logarithm $\log(F(\cdot))$ is interpolated instead of $F(\cdot)$ itself. Since $F(\cdot)$ versus n has an exponential-like shape, its logarithm is approximately a straight line, which can be interpolated with much less error. Fig. D.1 and Fig. D.2 demonstrate the accuracy of the different implementations of Gauss' hypergeometric function as a direct sum in (D.3) or as a recursion (D.4) with interpolation. It can be seen that an enormous error ($\sim$ 100dB) might be avoided, particularly if both parameter ρ and n are relatively large. This is exactly the case in along-track interferometry.

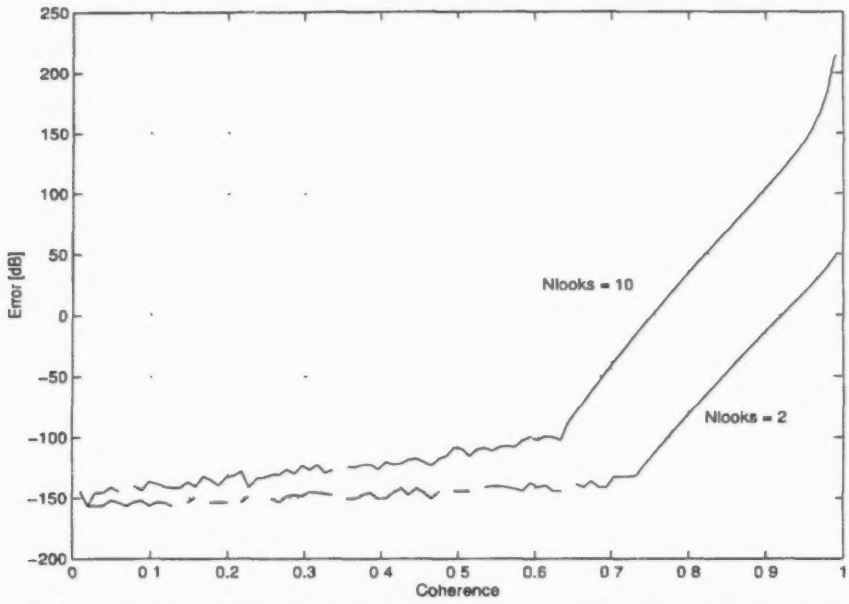

Figure D.1 : *Error of direct-sum implementations of Gauss hypergeometric function versus coherence for integral number of looks.*

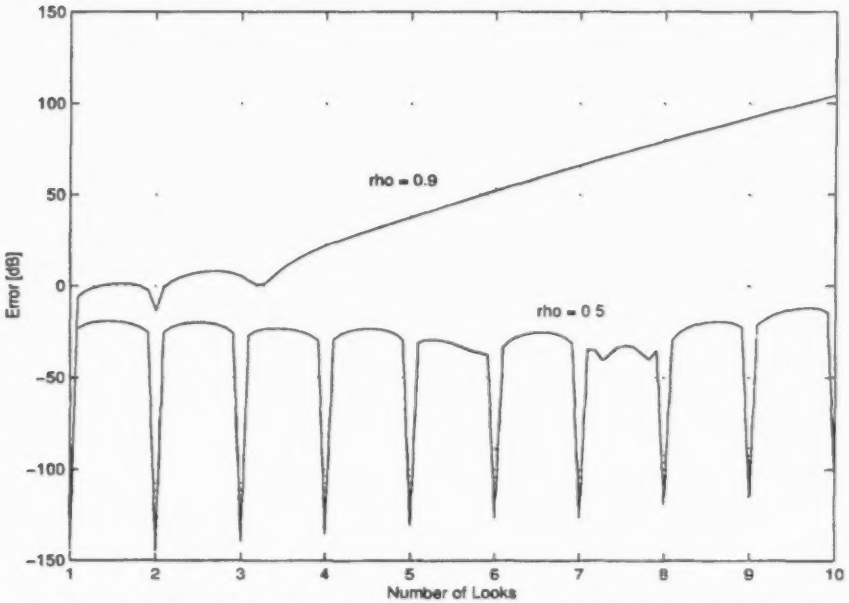

Figure D.2 : *Error of direct-sum implementations of Gauss hypergeometric function versus number of looks for different coherences.*

UNCLASSIFIED
SECURITY CLASSIFICATION OF FORM
(highest classification of Title, Abstract, Keywords)

DOCUMENT CONTROL DATA

(Security classification of title, body of abstract and indexing annotation must be entered when the overall document is classified)

1. ORIGINATOR (the name and address of the organization preparing the document Organizations for whom the document was prepared, e.g Establishment sponsoring a contractor's report, or tasking agency, are entered in section 8.)

DEFENCE RESEARCH ESTABLISHMENT OTTAWA
DEPARTMENT OF NATIONAL DEFENCE
OTTAWA, ONTARIO, CANADA, K1A 0K2

2. SECURITY CLASSIFICATION (overall security classification of the document, including special warning terms if applicable)

UNCLASSIFIED

3. TITLE (the complete document title as indicated on the title page. Its classification should be indicated by the appropriate abbreviation (S,C or U) in parentheses after the title.)

STATISTICS OF SAR INTERFEROGRAMS WITH APPLICATION TO MOVING TARGET DETECTION (U)

4. AUTHORS (Last name, first name, middle initial)

GIERULL, CHRISTOPH, H.

5. DATE OF PUBLICATION (month and year of publication of document)	6a. NO OF PAGES (total containing information. Include Annexes, Appendices, etc.)	6b. NO. OF REFS (total cited document)
JUNE 2001	64	28

7. DESCRIPTIVE NOTES (the category of the document, e.g technical report, technical note or memorandum. If appropriate, enter the type of report, e.g. interim, progress, summary, annual or final. Give the inclusive dates when a specific reporting period is covered.)

DREO REPORT

8. SPONSORING ACTIVITY (the name of the department project office or laboratory sponsoring the research and development. Include the address.)

DEFENCE RESEARCH ESTABLISHMENT OTTAWA
DEPARTMENT OF NATIONAL DEFENCE
OTTAWA, ONTARIO, CANADA, K1A 0K2

9a. PROJECT OR GRANT NO. (If appropriate, the applicable research and development project or grant number under which the document was written. Please specify whether project or grant)	9b. CONTRACT NO. (If appropriate, the applicable number under which the document was written)
3DB29	

10a. ORIGINATOR'S DOCUMENT NUMBER (the official document number by which the document is identified by the originating activity. This number must be unique to this document.)	10b. OTHER DOCUMENT NOS. (Any other numbers which may be assigned this document either by the originator or by the sponsor)
DREO TECHNICAL REPORT 2001- 045	

11. DOCUMENT AVAILABILITY (any limitations on further dissemination of the document, other than those imposed by security classification)

(X) Unlimited distribution
( ) Distribution limited to defence departments and defence contractors; further distribution only as approved
( ) Distribution limited to defence departments and Canadian defence contractors; further distribution only as approved
( ) Distribution limited to government departments and agencies; further distribution only as approved
( ) Distribution limited to defence departments; further distribution only as approved
( ) Other (please specify):

12. DOCUMENT ANNOUNCEMENT (any limitation to the bibliographic announcement of this document. This will normally correspond to the Document Availability (11). However, where further distribution (beyond the audience specified in 11) is possible, a wider announcement audience may be selected.)

P516111.PDF [Page: 68 of 69]

13. ABSTRACT (a brief and factual summary of the document. It may also appear elsewhere in the body of the document itself. It is highly desirable that the abstract of classified documents be unclassified. Each paragraph of the abstract shall begin with an indication of the security classification of the information in the paragraph (unless the document itself is unclassified) represented as (S), (C), or (U). It is not necessary to include here abstracts in both official languages unless the text is bilingual).

(U) This report examines the statistics of the phase and magnitude of SAR interferograms towards the deployment of along-track interferometry (ATI) for slow ground moving target indication (GMTI). Great importance is attached to the practical applicability of the derived theoretical results, particularly with regard to the experimental MTI-mode of Radarsat2. Therefore, the results are evaluated with experimental airborne SAR data acquired during flight trials conducted in Petawawa in 1999. While the known probability density function (pdf) of the interferogram's phase (derived under the assumption of Gaussian backscatter) is shown to agree almost perfectly for a wide variety of backscatter conditions, the corresponding magnitude's pdf tends to deviate strongly in most cases. Motivated by this discrepancy, a novel distribution is derived for the interferogram's magnitude. This pdf, called the polynomial or p-distribution, matches the real data much more accurately, particularly for extremely heterogeneous composite terrain. Based on these statistics, a completely automatic detection scheme with constant false alarm rates for slow moving targets is proposed. All involved parameters required to determine the detection thresholds are estimated from the sample data. It is demonstrated on the basis of a real SAR scene that this detector is capable of detecting slow moving vehicles within severe ground clutter. Finally, practical aspects of the implementation and numerical stability are addressed, since many of the functions involved are comprised of indefinite power series which have to be handled cautiously.

14. KEYWORDS, DESCRIPTORS or IDENTIFIERS (technically meaningful terms or short phrases that characterize a document and could be helpful in cataloguing the document. They should be selected so that no security classification is required. Identifiers such as equipment model designation, trade name, military project code name, geographic location may also be included. If possible keywords should be selecte from a published thesaurus. e.g. Thesaurus of Engineering and Scientific Terms (TEST) and that thesaurus-identified. If it is not possible to select indexing terms which are Unclassified, the classification of each should be indicated as with the title.)

ALONG-TRACK INTERFEROMETRY
GROUND MOVING TARGET INDICATION
STATISTICS OF SAR INTERFEROGRAMS

P516111.PDF [Page: 69 of 69]

Defence R&D Canada
is the national authority for providing
Science and Technology (S&T) leadership
in the advancement and maintenance
of Canada's defence capabilities.

R et D pour la défense Canada
est responsable, au niveau national, pour
les sciences et la technologie (S et T)
au service de l'avancement et du maintien des
capacités de défense du Canada.

516111
CA011559

DEFENCE R&D DÉFENSE

www.drdc-rddc.dnd.ca